

# Deep spectroscopy of distant 3CR radio galaxies: the data

P. N. Best,<sup>1\*</sup> H. J. A. Röttgering<sup>1</sup> and M. S. Longair<sup>2</sup>

<sup>1</sup> *Sterrewacht Leiden, Postbus 9513, 2300 RA Leiden, the Netherlands*

<sup>2</sup> *Cavendish Astrophysics, Madingley Road, Cambridge, CB3 0HE, UK*

23 July 2021

## ABSTRACT

Deep long-slit spectroscopic data are presented for a sample of 14 3CR radio galaxies at redshift  $z \sim 1$ , previously studied in detail using the Hubble Space Telescope, the Very Large Array, and UKIRT. Analysis of the [OII] 3727 emission line structures at  $\sim 5\text{\AA}$  spectral resolution is carried out to derive the kinematic properties of the emission line gas. In line with previous, lower resolution, studies, a wide variety of kinematics are seen, from gas consistent with a mean rotational motion through to complex structures with velocity dispersions exceeding  $1000\text{ km s}^{-1}$ . The data confirm the presence of a high velocity gas component in 3C265 and detached emission line systems in 3C356 and 3C441, and show for the first time that the emission line gas in the central regions of 3C324 is composed of two kinematically distinct components. Emission line fluxes and the colour of the continuum emission are determined down to unprecedentedly low observed wavelengths,  $\lambda < 3500\text{\AA}$ , sufficiently short that any contribution of an evolved stellar population is negligible. An accompanying paper investigates the variation in the emission line ratios and velocity structures within the sample, and draws conclusions as to the origin of the ionisation and kinematics of these galaxies.

**Key words:** Galaxies: active — Galaxies: interstellar medium — Radio continuum: galaxies — Galaxies: Individual: 3C324, 3C265

## 1 INTRODUCTION

The emission line properties of powerful distant ( $z \gtrsim 0.5$ ) radio galaxies are striking. Their emission line luminosities are large, with the rest-frame equivalent width of the [OII] 3727 line frequently exceeding  $100\text{\AA}$  (e.g. Spinrad 1982). Indeed, the strong correlation between emission line luminosity and radio power (e.g. Rawlings & Saunders 1991) was the key factor in enabling spectroscopic completeness to be achieved for a large sample of powerful radio galaxies (the revised 3CR catalogue; Laing et al. 1983). The line emission of the distant 3CR radio galaxies is also seen to be spatially extended over regions that can be as large as 100 kpc and is frequently elongated along the direction of the radio axis (e.g. McCarthy 1988, McCarthy et al. 1995).

The source of ionisation of this gas has been a long standing question. Robinson et al. (1987) found that optical emission line spectra of most low redshift ( $z \lesssim 0.1$ ) radio galaxies are well explained using photoionisation models, and a similar result was found for a composite spectrum of radio galaxies with redshifts  $0.1 < z < 3$  (McCarthy 1993). Photoionisation models are also supported by orientation-

based unification schemes of radio galaxies and radio-loud quasars (e.g. Barthel 1989), in which all radio galaxies host an obscured quasar nucleus: the flux of ionising photons required to produce the observed luminosities of the emission line regions can be shown to be comparable to that produced by radio-loud quasars at the same redshift (e.g. see McCarthy 1993). On the other hand, detailed studies of individual sources (e.g. 3C277.3; van Breugel et al 1985; 3C171; Clark et al. 1998) have revealed features such as enhanced nebular line emission, high velocity gas components, and large velocity dispersions coincident with the radio hotspots or with bends in the radio jets, indicating that the morphology and kinematics of the gas in some sources are dominated by shocks associated with the radio source. The ionisation state of the gas in these regions is also consistent with that expected from shock ionisation (e.g. Villar-Martín et al. 1999). Bicknell et al. (1997) considered the energy input to the emission line regions of Gigahertz-Peaked Spectrum (GPS) and Compact Steep Spectrum (CSS) sources from the shocks associated with the advance of the radio jet and cocoon, and showed that the energy supplied by the shocks to the interstellar medium is sufficient to account for the observed line emission. The relative importance of shocks and photoionisation in producing the emission line proper-

\* Email: pbest@strw.leidenuniv.nl

ties of the general radio galaxy population therefore remains an open question.

Another important issue is the varied kinematics seen in the emission line regions. At low redshifts the emission line properties of the 3CR radio galaxies have been intensively studied (e.g. Baum et al. 1992 and references therein); a variety of kinematics are seen, from galaxies consistent with simple rotation through to those classified as ‘violent non-rotators’ with large turbulent velocities. At higher redshifts, McCarthy et al. (1995; 1996) have studied a large sample of 3CR radio galaxies with low spectral and spatial resolution, and find that the velocity full-width-half-maxima (FWHM) are significantly higher than those at low redshifts (see also Baum et al. 1998), often exceeding  $1000 \text{ km s}^{-1}$ , and large velocity shears are seen. The exceptional nature of the kinematics has been reinforced by more detailed studies of individual sources (e.g. Spinrad & Djorgovski 1984, Tadhunter 1991, Meisenheimer & Hippelein 1992, Hippelein & Meisenheimer 1992, Stockton et al. 1996, Neeser et al. 1997). The emission line properties of these high redshift radio galaxies are evidently more extreme than those at low redshift (and hence of lower radio power) in more than just their luminosities.

The origin of the emission line gas itself is another unresolved issue. Typically  $10^8$  to  $10^9 M_{\odot}$  of ionised gas are estimated to be present around these objects (McCarthy 1993 and references therein), significantly more than found in quiescent low redshift ellipticals. The gas may have an origin external to the radio galaxy, being either associated with the remnants of a galaxy merger (Heckman et al. 1986; Baum & Heckman 1989), or gas brought in by a massive cooling flow in a surrounding intracluster medium; some support for the latter hypothesis is given by the detection of extended X-ray emission around a number of powerful distant radio galaxies (Crawford and Fabian 1996 and references therein), although the higher than primordial metallicity of the gas (as indicated by the strong emission lines of, for example, oxygen, neon, magnesium and sulphur) dictates that the gas must have been processed within stars at some point in its past. Alternatively, the gas may be left over from the formation phase of these massive galaxies, perhaps expelled from the galaxy either in a wind following an earlier starburst phase or more recently by the shocks associated with the radio source. If the gas has an origin external to the host galaxy, then it is important to know what the connection is, if any, between the origin of this gas and the onset of the radio source activity.

The properties of the continuum emission of powerful distant radio galaxies are equally interesting. At near infrared wavelengths the galaxies follow a tight  $K-z$  Hubble relation (Lilly & Longair 1984) and their host galaxies have colours and radial light profiles consistent with being giant elliptical galaxies which formed at large redshifts (Best et al. 1998b). At optical wavelengths, however, powerful radio galaxies beyond redshift  $z \sim 0.6$  show a strong, but variable, excess of blue emission, generally aligned along the radio axis (McCarthy et al. 1987; Chambers et al. 1987). Using Hubble Space Telescope (HST) images of a sample of 3CR radio galaxies with redshifts  $z \sim 1$ , we have shown that the nature of this alignment differs greatly from galaxy to galaxy, in particular becoming weaker as the linear size of the radio source increases (Best et al. 1996; Best et al.

1997). It is clear that a number of different physical processes contribute to the continuum alignment effect, but less clear which processes are the most important (for reviews see e.g. McCarthy 1993, Röttgering & Miley 1996).

To study the emission line gas properties of these galaxies, our multi-waveband imaging project on the redshift one 3CR galaxies has been expanded to include deep spectroscopic observations, producing a combined dataset of unparalleled quality. In the current paper the basic results of the spectroscopic program are presented. The layout is as follows. In Section 2, details concerning the sample selection, the observations and the data reduction are presented. Section 3 contains the direct results of these observations, in the form of extracted one-dimensional spectra, two-dimensional studies of the [OII] 3727 emission line structures, tables of spectral properties, and a brief description of the individual sources. The results are summarised in Section 4. An accompanying paper (Best et al 1999; hereafter Paper 2) investigates the emission line ratios and velocity structures of the sample as a whole, and the consequences of these for the origin of the ionisation and kinematics of these galaxies. A later paper will address the nature of the continuum emission.

Throughout the paper, values of the cosmological parameters of  $\Omega = 1$  and  $H_0 = 50 \text{ km s}^{-1} \text{ Mpc}^{-1}$  are assumed. For this cosmology, 1 arcsec corresponds to 8.5 kpc at redshift  $z = 1$ .

## 2 OBSERVATIONAL DETAILS

### 2.1 Sample selection and observational set-up

The galaxies were drawn from the essentially complete sample of 28 3CR radio galaxies with redshifts  $0.6 < z < 1.8$  which we have intensively studied using the HST, the VLA and UKIRT (e.g. Best et al. 1997). From this sample, spectroscopic studies were restricted initially to those 18 galaxies with redshifts  $0.7 < z < 1.25$ , the upper redshift cut-off corresponding to that at which the  $4000\text{\AA}$  break is redshifted beyond an observed wavelength of  $9000\text{\AA}$  and the lower redshift cut-off being set by telescope time limitations. Of these 18 galaxies, 3C41 ( $z = 0.795$ ), 3C65 ( $z = 1.176$ ), 3C267 ( $z = 1.144$ ) and 3C277.2 ( $z = 0.766$ ) were subsequently excluded. In the cases of 3C65 and 3C267, their exclusion was due to partially cloudy conditions during one observing night resulting in a poor data quality for these two observations. The omission of 3C41 and 3C277.2 was due to constraints of telescope time at the relevant right ascensions: the decision not to observe these particular two galaxies was based solely upon them having the lowest redshifts in the sample at those right ascensions. The exclusion of these four galaxies should not introduce any significant selection effects.

The remaining 14 galaxies were observed on July 7-8 1997 and February 23-24 1998, using the dual-beam ISIS spectrograph on the William Herschel Telescope (WHT). The  $5400\text{\AA}$  dichroic was selected since it provided the highest throughput at short wavelengths. The R158B grating was used in combination with a Loral CCD in the blue arm of the spectrograph. This low spectral resolution ( $\sim 12\text{\AA}$ ) grating provided the largest wavelength coverage ( $3700\text{\AA}$ )

and maximized the signal-to-noise at short wavelengths by decreasing the importance of the CCD read-out noise, which even still was the dominant source of noise at wavelengths below about  $3400\text{\AA}$ . This set-up enabled accurate measurement of many emission line strengths and a determination of the slope of the continuum emission at sufficiently short wavelengths that any contribution of the evolved stellar population will be negligible; at such wavelengths the spectral characteristics of the aligned emission alone are measured and can be used to pin down the physical processes contributing to the alignment effect. During the July run, the wavelength range sampled by the CCD was set to span from below the minimum useful wavelength ( $\sim 3250\text{\AA}$ ) to longward of the dichroic. During the February run, the (different) Loral CCD had a charge trap in the dispersion direction at about pixel 1000, reducing the credibility of data at longer wavelengths; the wavelength range was tuned to sample from  $3275\text{\AA}$  up to the charge trap at about  $5100\text{\AA}$ .

In the red arm of the spectrograph the R316R grating was used in combination with TEK CCD, providing a spatial scale of 0.36 arcsec per pixel, a dispersion of  $1.49\text{\AA}$  per pixel and a spectral resolution of about  $5\text{\AA}$ . The wavelength range of about  $1500\text{\AA}$  was centred on the wavelength given in Table 1 for each galaxy, tuned to cover as much as possible of the range from approximately  $3550\text{\AA}$  to  $4300\text{\AA}$  in the rest-frame of the galaxy whilst remaining below a maximum observed wavelength of  $9000\text{\AA}$ . This higher spectral resolution set-up in the red arm allows a much more detailed investigation of the velocity structures of the emission line gas as seen in the very luminous [OII] 3727 emission line, but still provides sufficient wavelength coverage to include the  $4000\text{\AA}$  break, the Balmer continuum break at  $3645\text{\AA}$  and a number of Balmer emission lines.

## 2.2 Observations and data reduction

Long-slit spectra of the 14 galaxies were taken with total integration times of between 1.5 and 2 hours per galaxy; the observations were split between 3 or 4 separate exposures in the red arm to assist in the removal of cosmic rays; the blue arm observations were split between only 2 exposures since shorter exposures would have had a more significant read-noise contribution. The slit was orientated either along the radio axis or along the axis of elongation of the optical-UV emission. Full details of the observations are provided in Table 1.

The seeing was typically 0.8 to 1 arcsec during the July run, and between 1 and 1.25 arcsec during the February observations. The first half of the February 23 night was partially cloudy, hampering the observations of 3C65 and 3C267 as discussed above. The observations of 3C217 *may* have suffered partial cloud interference and be non-photometric, although the approximate agreement between the  $7500\text{\AA}$  flux density determined from the spectrum and that extracted from the equivalent region of an HST image of this galaxy, convolved to the same angular resolution, suggest that this was not significant. Conditions during the second half of that night and the other three nights were photometric.

The data were reduced using standard packages within the IRAF NOAO reduction software. The raw data frames were corrected for overscan bias, and flat-fielded using observations of internal calibration lamps with the same instrumen-

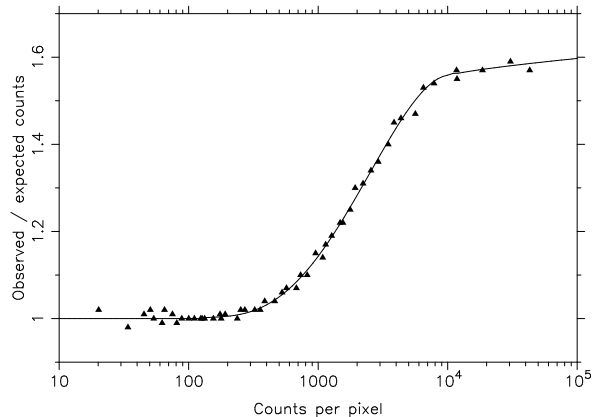


**Figure 1.** The non-linearity of the Loral CCD during the July run. The ‘expected’ counts were determined by defining (arbitrarily) for a given CCD region the frame in the exposure time sequence of flat field frames (see text) that gave just over 100 counts per pixel to be ‘correct’, and scaling the expected counts for other frames by their exposure time; hence the string of 1.00’s from 100 to 150 counts. The solid line represents a polynomial fit to the data points.

tal set-up as the object exposures: ie. in the red arm, separate flat fields were constructed for each galaxy, since each was observed with a different *observed* wavelength range; these flat field observations were interspersed with the series of on-source exposures to minimise fringing effects. The sky background was removed, taking care not to include extended line emission in the sky bands. The different exposures of each galaxy were then combined, removing the cosmic ray events, and one dimensional spectra were extracted. The data were wavelength calibrated using observations of CuNe and CuAr arc lamps, and accurate flux calibration was achieved using observations of the spectrophotometric standard stars GD190, EG79, G9937 and LDS749b, again observed using exactly the same instrumental setup as each galaxy and corrected for airmass extinction.

## 2.3 The non-linearity of the Loral CCD

The far greater efficiency of the Loral CCD at wavelengths below  $4000\text{\AA}$  than any other CCD available at the time of these observations ( $\approx 75\%$  as compared with  $\approx 35\%$  quantum efficiency at  $3500\text{\AA}$ ) offered an unrivalled opportunity for study at these wavelengths. However, the Loral CCD used during the July run had a slightly non-linear response curve, giving rise to a minor problem concerning flux calibration of the blue arm data from this run. In order to assess the extent of this problem, a sequence of flat field observations of the internal calibration lamps were taken, with exposures of 0, 1, 2, 3, 5, 7, 10, 15, 20, 30, 60, 120, 300, 120, 60, 30, 20, 15, 10, 7, 5, 3, 2, 1, 0 seconds, the average of the frames for each exposure time on the increasing and decreasing exposure time branches being taken to account for any systematic time variation in the intensity of the calibration lamp. A small (relatively uniform intensity) region of the CCD was selected and, after subtraction of the 0 second bias frame, the mean counts per pixel in that region was measured for each different exposure time frame. The frame providing on average just over 100 counts per pixel

**Table 1.** Details of the ISIS observations.

Source	Observ. Date	Slit width ["]	Exp. Time Red Arm [s]	Exp. Time Blue Arm [s]	Red Arm Cen. $\lambda$ [Å]	Slit PA [deg.]	Notes
3C22	07/07/97	1.50	5400	5400	7645	103	[1]
3C217	23/02/98	1.54	7250	7200	7625	90	[2,3]
3C226	23/02/98	1.54	7200	7200	7260	145	[1]
3C247	24/02/98	1.70	6600	6660	7100	70	[1]
3C252	24/02/98	1.75	7140	7200	8235	105	[1]
3C265	23/02/98	1.54	5500	5500	7260	136	[4]
3C280	07/07/97	1.50	5400	5400	7860	90	[1]
3C289	08/07/97	1.50	2700	2700	7760	109	[1]
3C289	23/02/98	1.54	2200	2200	7820	109	[1]
3C324	07/07/98	1.50	5400	5400	7860	90	[1]
3C340	24/02/98	1.75	6900	7000	7105	85	[1]
3C352	08/07/98	1.50	5400	5400	7170	161	[1]
3C356	07/07/98	1.50	5400	5400	7860	147	[5]
3C368	08/07/98	1.50	5400	5400	8235	10	[1]
3C441	08/07/98	1.50	5400	5400	6830	150	[1]

[1] Slit aligned along the radio axis.

[2] Slit aligned intermediately between the radio axis ( $104^\circ$ ) and the elongation of the central optical knots ( $75^\circ$ ).

[3] Observations may be non-photometric (see text).

[4] Slit aligned along the extended UV emission, rather than the radio axis which has a PA of  $106^\circ$ .

[5] Slit aligned to include both of the two central galaxies; slightly offset from the true radio PA of  $160^\circ$ .

was arbitrarily declared to be ‘correct’; the ‘expected’ count level for this CCD region in the other frames was then calculated by scaling by the exposure time, and compared to the observed counts. This process was repeated for a large number of different regions on the CCD, and also with a smaller sample of flat-field observations taken the following night.

The results of this analysis are presented in Figure 1, which shows that the Loral CCD is non-linear at the  $\lesssim 10\%$  level at count levels below  $\sim 800$  counts per pixel, but above that level the non-linearity increases sharply. The scatter around a parameterised fit to the non-linearity curve in the 300 to 500 counts range can be explained by Poisson noise statistics alone, indicating that the non-linearity was highly repeatable, varying neither with time nor with position on the CCD, and thus allowing the small non-linearity at these count levels to be accurately calibrated out.

The faintness of the radio galaxies being studied meant that the detected counts per pixel in the on-source exposures, including both sky and object counts, fell automatically within the range 50 to 800 counts per pixel. Both the flat field and the standard star exposures in the blue arm during the July run were built up by summing a series of images, each of which was kept short to have maximum count levels below 1000 counts per pixel. The parameterised curve shown in Figure 1 was then divided into the scientific exposures, after bias subtraction but before flat fielding and other calibration. Such a correction was also applied to the flat-field exposures and to the observations of standard stars. In this way, any systematic offset introduced by the application of the non-linearity curve to the object will be roughly cancelled by its application to the calibrator, reducing any errors to  $\lesssim 2\%$ , far below the other uncertainties related to the calibration procedure.

**Table 2.** Spectroscopic properties of the radio galaxies. The [OII] 3727 integrated flux (measured within or scaled to a 1.5 arcsec slit width), in units of  $10^{-16} \text{ erg s}^{-1} \text{ cm}^{-2}$ , corresponds to the line flux along the entire length of the slit calculated by integrating the [OII] 3727 intensities shown in Figures 2-15(d). All of the flux ratios and flux densities quoted in this table are corrected for galactic extinction using the E(B-V) for the Milky Way from Burstein & Heiles (1982) and the parameterised galactic extinction law of Howarth (1983). All flux ratios are measured relative to [OII] 3727 (value of 100) within the extracted 1-dimensional spectrum. The error on the [OII] 3727 line flux is dominated by calibration errors which are estimated to be  $\lesssim 10\%$ . Errors in the other flux ratios take account of both the errors due to photon statistics and a 10% calibration uncertainty. Note that there might be a small  $\lesssim 5 - 10\%$  systematic offset between the blue and red arm measurements due to different spatial extraction regions (the spatial extraction length is the same in both arms, but might be centred slightly differently). Also, since the slit position angles were different from the parallactic angle, differential refraction may result in the galaxy not being completely centred in the slit at both the red and blue extremes. This latter effect should be minimal, however, as it was ensured that all observations were taken either at low airmass or with the slit position angle close to the parallactic angle). Equivalent widths are measured in the rest-frame of the galaxy. Mean flux densities for given line-free wavelength ranges (or as much of the range as possible provided at least  $100\text{\AA}$  are covered in the spectrum) are measured from the extracted one-dimensional spectrum; the (weak)  $H\delta$  emission line was subtracted before calculating the mean continuum level for the wavelength range 4050-4250Å. Values are in units of  $10^{-18} \text{ erg s}^{-1} \text{ cm}^{-2} \text{ \AA}^{-1}$ ; the uncertainty given is the error on the mean value in that wavelength region. Notes: [1] values are quoted separately for the northern and southern host galaxy candidates for 3C356; [2] for 3C368, due to the presence of a galactic M-star coincident with the galaxy (Hammer et al. 1991), the equivalent widths are strictly lower limits and continuum flux densities have not been measured; [3] for 3C441 the values quoted do not include the companion galaxy; [4] the red arm spectra do not reach sufficiently high rest-frame wavelengths.

Source	3C22	3C217	3C226	3C247	3C252	3C265	3C280	3C289	3C324	3C340	3C352	3C356(N) <sup>1</sup>	3C356(S) <sup>1</sup>	3C368 <sup>2</sup>	3C441 <sup>3</sup>	
Redshift	0.935	0.898	0.818	0.749	1.104	0.810	0.997	0.967	1.208	0.775	0.806	1.079	1.084	1.132	0.708	
Milky Way E(B-V)	0.24	0.01	0.01	0.00	0.00	0.00	0.00	0.01	0.03	0.03	0.02	0.02	0.02	0.18	0.09	
Integrated [OII] 3727 flux	20.2	48.5	12.1	12.4	8.1	35.6	21.1	7.8	19.3	5.8	25.7	7.6	7.4	58.7	4.7	
CIV 1549	Flux ratio	—	—	—	—	—	—	—	19	—	—	—	—	—	—	
	Error	—	—	—	—	—	—	—	3	—	—	—	—	—	—	
	Equiv. width	—	—	—	—	—	—	—	32	—	—	—	—	—	—	
HeII 1640	Flux ratio	—	—	—	—	76	—	51	14	—	—	57	40	8.7	—	
	Error	—	—	—	—	8	—	9	1.6	—	—	7	8	1.9	—	
	Equiv. width	—	—	—	—	51	—	70	26	—	—	68	81	23	—	
CIII] 1909	Flux ratio	30	14	16	22	44	64	34	36	18	122	16	58	20	18	
	Error	3	2	3	7	5	7	4	4	2	20	2	6	4	1.4	
	Equiv. width	10	72	15	70	35	35	52	86	41	136	55	73	63	60	
CII] 2326	Flux ratio	6.2	11	8.3	9.5	17	10	7.1	13	7.4	13	9.2	6.9	8.4	17	6.4
	Error	0.9	1	1.0	2.4	2.5	1	0.9	1.5	1.6	1.9	1.1	1.1	2.2	2.5	1.8
	Equiv. width	7	62	14	22	22	7	13	43	16	16	37	9	40	56	11
[NeIV] 2425	Flux ratio	15	4.7	19	2.4	26	34	16	12	—	32	3.1	27	—	4.5	7.9
	Error	1.6	0.6	2	0.9	5	4	2	1.5	—	4	0.5	3	—	1.6	1.6
	Equiv. width	9	24	27	12	28	25	27	31	—	36	13	34	—	16	12
MgII 2798	Flux ratio	—	18	—	5.5	—	25	—	—	—	28	17	—	—	—	5.1
	Error	—	2	—	1.6	—	5	—	—	—	4	2	—	—	—	2.0
	Equiv. width	—	115	—	31	—	20	—	—	—	33	66	—	—	—	6
[NeV] 3426	Flux ratio	—	—	—	—	—	—	—	—	8.3	—	—	—	—	—	—
	Error	—	—	—	—	—	—	—	—	1.0	—	—	—	—	—	—
	Equiv. width	—	—	—	—	—	—	—	—	17	—	—	—	—	—	—
[OII] 3727	Flux ratio	100	100	100	100	100	100	100	100	100	100	100	100	100	100	100
	Equiv. width	80	544	159	129	125	191	173	149	219	84	295	111	281	202	58
[NeIII] 3869	Flux ratio	36	16	29	12	48	34	35	7.2	51	39	22	56	16	22	25
	Error	4	2	3	1.6	5	3	4	1.6	6	4	2	6	3	2	3
	Equiv. width	30	89	47	31	57	78	62	10	121	33	62	58	34	41	13
Hζ 3889	Flux ratio	7.8	3.8	5.6	—	11	10	5.9	—	7.6	5.4	4.2	9.5	—	—	8.3
	Error	1.4	0.6	1.4	—	2.5	1	1.5	—	2.5	1.6	1.1	1.6	—	—	2.4
	Equiv. width	7	22	9	—	15	23	8	—	18	14	12	10	—	—	6
Hε + [NeIII] 3967	Flux ratio	12	8.8	11	—	20	14	17	13	—	18	7.3	21	6.3	6.1	4.8
	Error	1.6	1.0	2.4	—	3	1.5	2	1.5	—	2	0.8	3	1.7	0.7	0.8
	Equiv. width	10	56	18	—	29	36	28	16	—	14	20	21	11	12	3
Hδ 4102	Flux ratio	11	4.0	9.3	—	16	11	9.5	—	—	11	7.1	18	—	4.7	7.4
	Error	2	0.7	2.3	—	3	1.5	1.3	—	—	1.7	0.8	2	—	0.6	1.4
	Equiv. width	12	25	15	—	23	30	14	—	—	7	19	16	—	10	4
Hγ 4340	Flux ratio	29	12	16	1.6	—	19	—	17	—	29	13	—	—	—	18
	Error	4	1	3	0.7	—	2	—	3	—	4	1.8	—	—	—	3
	Equiv. width	18	64	26	8	—	52	—	13	—	17	38	—	—	—	9
Ca K 3933 (absorp.)	Equiv width	—	< 5	13	17	< 6	8	< 5	23	—	22	29	23	< 4	—	32
4000Å break strength		1.31	1.13	1.08	1.62	0.99	0.86	1.28	1.38	— <sup>4</sup>	1.52	1.17	— <sup>4</sup>	— <sup>4</sup>	—	1.64
	Error	0.03	0.11	0.07	0.06	0.11	0.05	0.09	0.08	—	0.07	0.04	—	—	—	0.04
Mean flux density	1670–1890Å	16.4	5.72	—	—	4.59	—	4.80	1.62	3.50	—	—	3.04	1.11	—	—
	Error	1.0	0.71	—	—	0.17	—	0.25	0.31	0.17	—	—	0.17	0.25	—	—
Mean flux density	2100–2300Å	13.4	4.17	3.73	2.63	4.23	17.55	4.04	1.47	2.78	2.36	2.71	2.76	0.47	—	1.94
	Error	0.2	0.15	0.16	0.13	0.09	0.16	0.07	0.07	0.09	0.15	0.12	0.05	0.09	—	0.17
Mean flux density	2450–2700Å	10.4	4.23	4.18	2.55	—	14.49	4.17	1.67	—	2.78	2.41	—	—	—	1.66
	Error	0.2	0.15	0.17	0.09	—	0.16	0.13	0.13	—	0.11	0.09	—	—	—	0.10
Mean flux density	3500–3700Å	7.15	—	3.86	—	3.14	6.54	4.34	2.22	3.75	3.93	3.90	3.41	1.00	—	3.57
	Error	0.06	—	0.21	—	0.20	0.20	0.14	0.09	0.12	0.18	0.09	0.07	0.17	—	0.09
Mean flux density	4050–4250Å	8.39	3.88	3.85	8.79	3.03	4.65	4.60	3.55	—	5.37	4.10	4.20	1.52	—	5.98
	Error	0.11	0.31	0.19	0.15	0.26	0.20	0.23	0.16	—	0.17	0.10	0.22	0.38	—	0.07

### 3 RESULTS

The resulting one dimensional spectra, extracted from the central 4.3 arcsec ( $\sim 35$  kpc) region along the slit direction in each of the blue and red arms, are shown in Figures 2 to 15 (a & b). In Table 2 are tabulated the fluxes of the various emission lines relative to [OII] 3727 and their equivalent widths, together with the mean flux density of the continuum in various wavelength regions. These flux ratios and flux densities (although not the plotted one-dimensional spectra, to allow comparison with previously published data) have been corrected for galactic extinction using the Milky Way HI column density data of Burstein and Heiles (1982), quoted in Table 2, and the parameterised galactic extinction law of Howarth (1983). These extinction corrections are  $\lesssim 10\%$  for most sources, but exceed a factor of 2 at the shortest wavelengths for the low galactic latitude source 3C22.

The emission line flux ratios and continuum flux densities are tabulated only for the single extracted spectrum. Even these very deep spectra do not have high enough signal-to-noise in the blue continuum of most of the galaxies to investigate in detail variations in the continuum colour along the spatial direction of the slit. Variations in the intensity, velocity and FWHM of the emission lines along the spatial direction of the slit are readily apparent, and are considered below in the study of the [OII] 3727 emission line.

Also presented in Table 2 are the observed strengths of the 4000Å break, as determined by the ratio of the mean *continuum* flux between 4050Å and 4250Å to that between 3750Å and 3950Å (Bruzual 1983); note that due to the presence of the excess aligned optical-UV emission, the strength of this break cannot be used directly to age the stellar populations of these galaxies, although the galaxies with only weak alignment effects (e.g. 3C441) do show fairly strong breaks indicative of evolved stellar populations.

To study the velocity structure of the [OII] 3727 emission line, a two-dimensional region around this emission line was extracted [Figures 2 to 15(c)], and from this a series of one dimensional spectra were extracted from spatial regions of width 4 pixels (1.44 arcsec), with the extraction centre stepped in units of 2 pixels (0.72 arcsec,  $\sim \frac{2}{3}$  of a seeing profile). Each extracted spectrum was then analysed using the following automated procedure.

(i) The extracted spectrum was fitted to find the best-fitting Gaussian, allowing for continuum subtraction. If this had a velocity FWHM greater than the instrumental resolution<sup>†</sup>, determined by measuring the FWHM of unblended sky lines, and had an integrated signal-to-noise ratio greater than 5 then it was accepted. Otherwise no fit was made at this spatial position.

(ii) The spectrum was then fitted using a combination of

two Gaussians. This fit was preferred to the single Gaussian fit only if both fitted Gaussians were wider than the velocity resolution, had an integrated signal-to-noise in excess of five, and the reduced chi-squared of two Gaussian fit was below that of the single Gaussian fit. If these requirements were not satisfied, the single Gaussian fit was adopted. Note that the amplitude of a fitted Gaussian was allowed to be negative to detect absorption features (although none were observed).

(iii) This process was repeated using 3,4,5 etc Gaussians.

In this way, it was possible to search for high velocity gas components, and structures in the emission line gas inconsistent with being a single velocity component (e.g. see 3C324; Figure 10). For each extracted Gaussian, the integrated emission line flux was calculated, as was the velocity relative to that at the centre of the galaxy and the FWHM of the emission line. The last of these was deconvolved by subtracting in quadrature the instrumental FWHM, as determined from unblended sky lines. The errors on each of these three parameters were also determined. It should be noted that a Gaussian did not always provide an ideal fit to the velocity profile, for example with profiles showing slight wings in either the blue or red direction, perhaps associated with a weaker emission component at a different velocity that was too faint to be individually distinguished.

The variation of the intensity, velocity and FWHM of the [OII] 3727 line emission with spatial location along the slit are presented in Figures 2 to 15(d to f). The large-scale variations in these three parameters measured here agree extremely well with those determined from lower spatial and spectral resolution data by McCarthy et al. (1996) for the seven galaxies in common between the two samples; the only significant exception is 3C324, where the higher spectral resolution of the current data has shown that a single Gaussian component is clearly not sufficient to describe the velocity structure. Note also that the surface brightnesses of the [OII] emission line determined from these spectra are comparable to those measured from the same region in narrow-band imaging of this emission line by McCarthy et al. (1995).

Important features of the emission line properties of individual galaxies are discussed briefly below. A full discussion of the continuum morphologies of these sources can be found in Best et al. (1997), and is not repeated here except where of direct relevance.

**3C22** has been identified as possessing a significant quasar component on the basis of a broad H $\alpha$  emission line and its high luminosity and nucleated appearance in the K-band (Dunlop & Peacock 1993; Rawlings et al. 1995; Economou et al. 1995). The emission line properties observed here, however, are by no means extreme (Figure 2). The [OII] line emission is confined to approximately the inner 2 arcsecond ( $\approx 17$  kpc) radial distance along the slit (see also McCarthy et al. 1995) and is consistent with velocity variations  $\lesssim 100$  km s<sup>-1</sup>. The FWHM seen for this line is high (700 to 800 km s<sup>-1</sup>) but not exceptional with respect to the rest of the sample. The ratio of emission line fluxes seen from this galaxy are intermediate within the sample, and similar to the combined radio galaxy spectrum of McCarthy (1993). The continuum emission at rest-frame wavelengths  $\lesssim 3000$ Å is somewhat bluer than average.

**3C217** possesses by far the highest equivalent width

<sup>†</sup> The exclusion on the basis of FWHM was necessary to avoid selection of single pixel spikes, but it should be noted that real features may have a measured FWHM less than the velocity resolution, and thus be excluded, if they are detected with only low signal-to-noise. However, all of the extracted Gaussian profiles are found to have deconvolved FWHM in excess of 200 km s<sup>-1</sup> (Figures 2 to 15f) and so it is extremely unlikely that any real features have been excluded by this method.

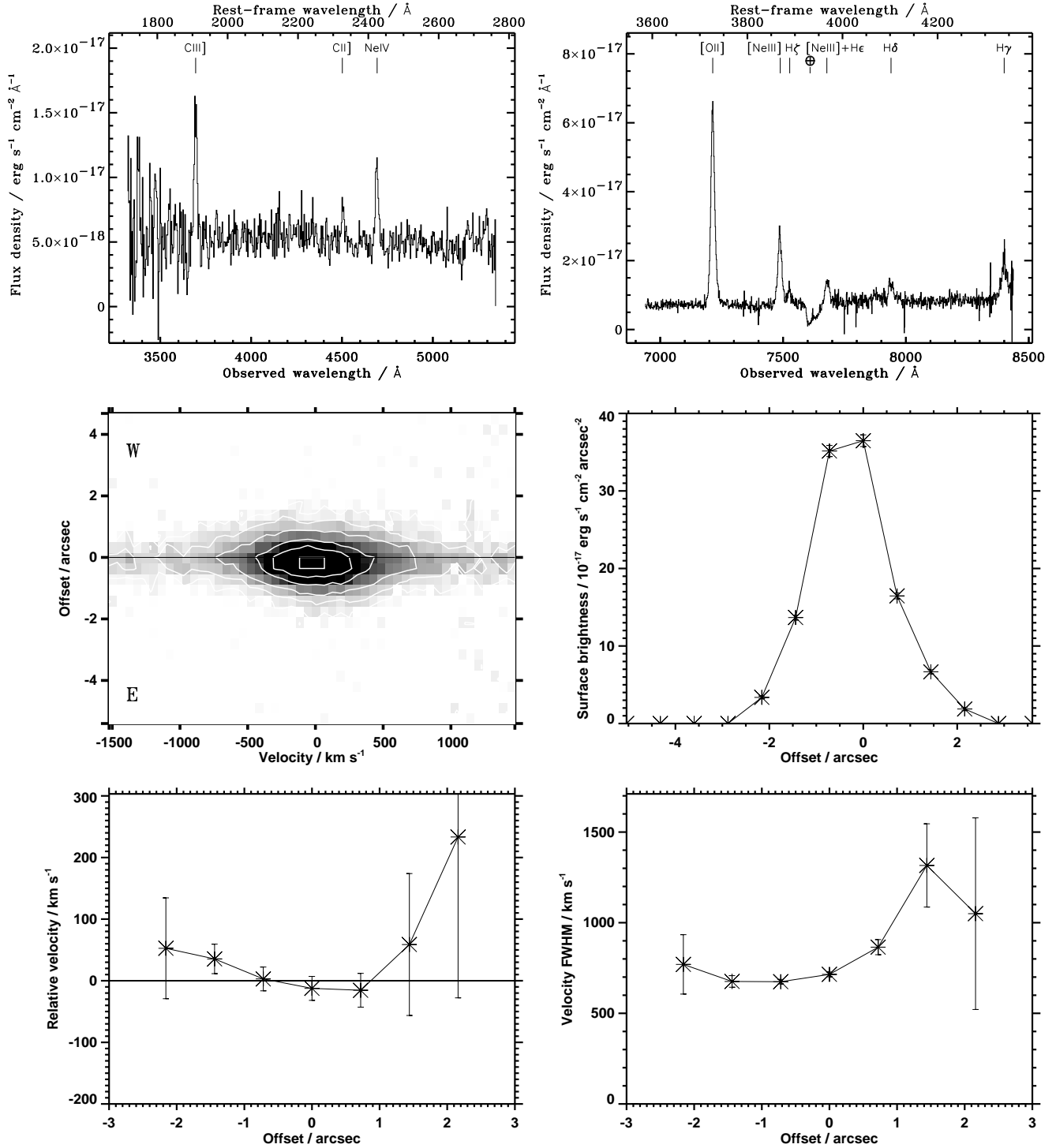


**Figure 2.** The spectroscopic data for **3C22**. (a – upper left) The extracted 1-dimensional blue arm spectrum. In this and in (b) the emission lines are labelled and sky features are indicated by an open circle with a cross. (b – upper right) The 1-dimensional spectrum extracted from the red arm. (c – middle left) The 2-dimensional [OII] 3727 emission line structure. Offset zero corresponds to the continuum centroid, and the sky directions of ‘positive’ and ‘negative’ slit offsets are indicated on the plot. (d – middle right) The surface brightness of the [OII] 3727 emission as a function of position along the slit. Where a second Gaussian component is fitted (see text; appropriate for later figures) this is plotted using open diamonds. (e – lower left) The velocity at the Gaussian peak of the [OII] 3727 emission as a function of position along the slit. (f – lower right) The variation of the FWHM of the fitted Gaussian profile as a function of position along the slit.

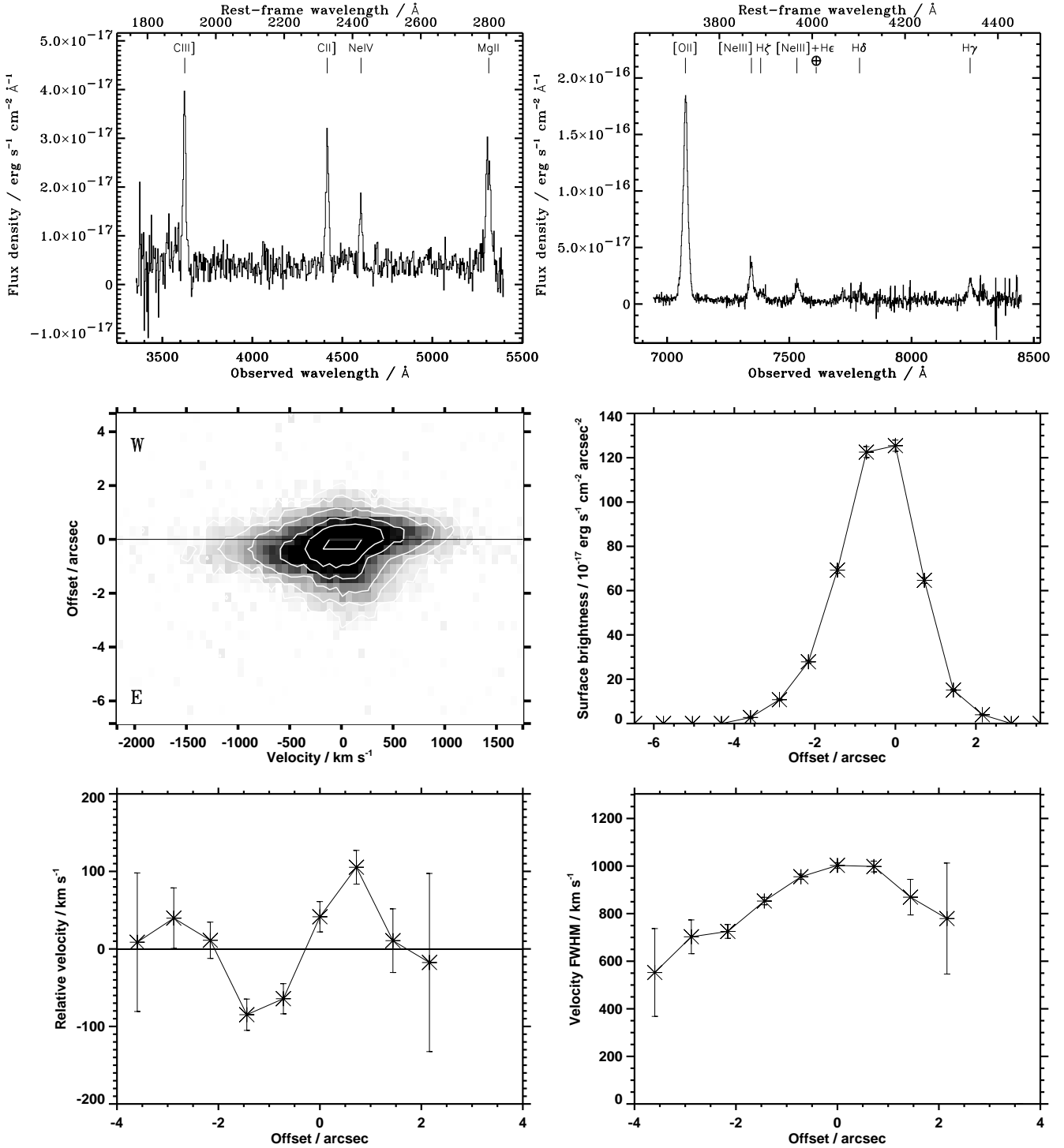


Figure 3. The spectroscopic data for 3C217. Details as in Figure 2.

[OII] 3727 line emission of all of the galaxies in this sample. This intense line emission is relatively compact (Figure 3; see also the narrow band [OII] 3727 image of Rigler et al. 1992) and confined to the inner 2–3 arcsec radius, in the region in which the HST images also show very luminous and blue rest-frame ultra-violet emission (Best et al. 1997). The [OII] line shows a large velocity dispersion and a complex velocity profile, but with only small ( $\lesssim 200 \text{ km s}^{-1}$ ) variations along

the slit in the mean velocity. Relative to the other galaxies in the sample, the lower ionisation lines are strong in the spectrum of this object.

3C226 shows a smooth, regular emission line gas profile (Figure 4). The [OII] 3727 emission line shows a clear intensity peak at the centre of the galaxy, extended slightly to the north-west (see also the narrow-band image of McCarthy et al. 1995) where the HST image shows a faint blue



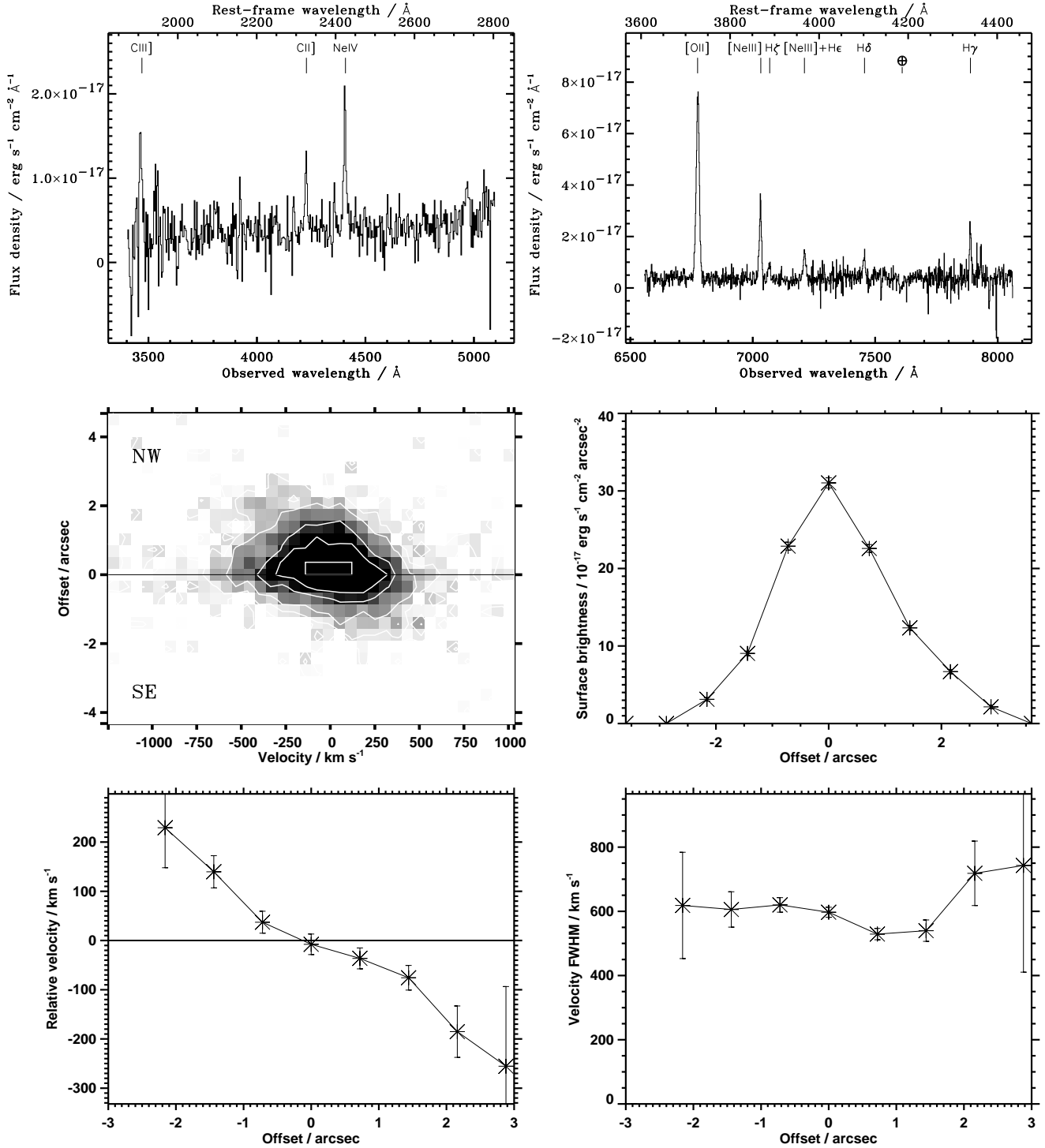


Figure 4. The spectroscopic data for 3C226. Details as in Figure 2.

knot of emission (Best et al. 1997). The relative velocity plot is consistent with a simple rotating halo; it may instead represent material infalling or outflowing along the radio axis, although the smooth slope of the velocity profile would be surprising in that case. The FWHM of the line profile is low relative to the other sources in the sample and fairly constant along the slit. At any given location along the slit, however, the dispersion in the line velocities is far greater

than the mean offset velocity of the emission line at that location, indicating that whether the relative velocity plot represents a mean rotational motion or if it arises through inflow or outflow of material, then there is considerable scatter in the emission line cloud velocities relative to these mean motions. The emission line ratios of 3C226 are fairly typical for the sample; the continuum emission in the blue-arm spectrum is redder than the average.

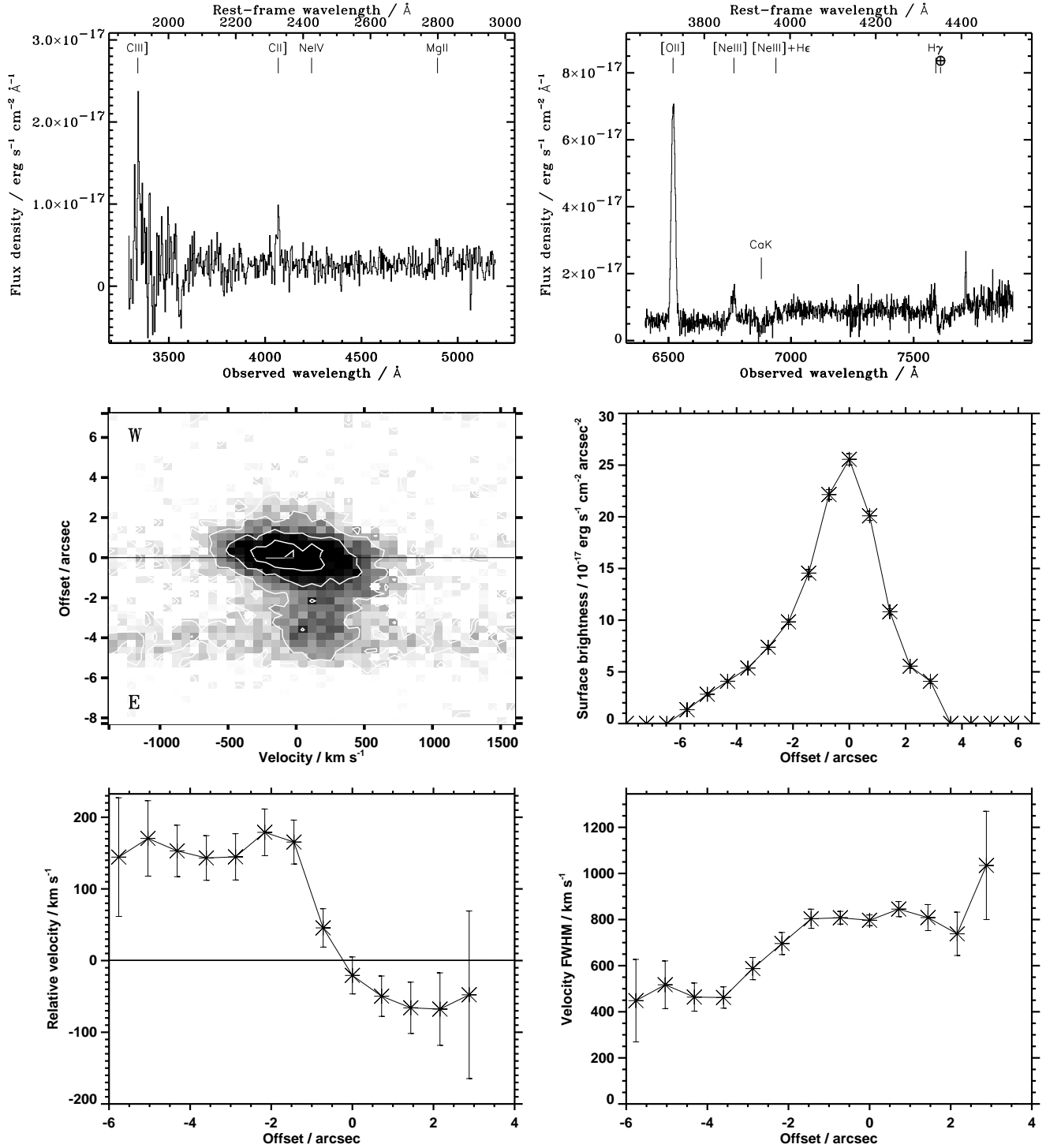


Figure 5. The spectroscopic data for 3C247. Details as in Figure 2.

3C247 has line emission extending for over 10 arcseconds along the radio axis (Figure 5; see also McCarthy et al. 1995). The inner approximately 2 arcsec radius of the line emission is almost symmetrical, with an intermediate velocity FWHM and a velocity profile which again may be consistent with a mean rotational motion or with infall/outflow of material. Further to the north-east there is a smooth transition into a region of [OII] emission red-

shifted by  $150 \text{ km s}^{-1}$  and with a lower velocity width. This second region has an associated continuum object, and it seems likely that what is seen here is an interaction of the radio galaxy with a companion. The radio galaxy itself shows a significant  $4000\text{\AA}$  break of strength  $1.61 \pm 0.06$ ; bearing in mind that the true strength of this break is diluted by aligned continuum emission, the host galaxy must contain a well-evolved stellar population. A strong CaK  $3933\text{\AA}$  ab-

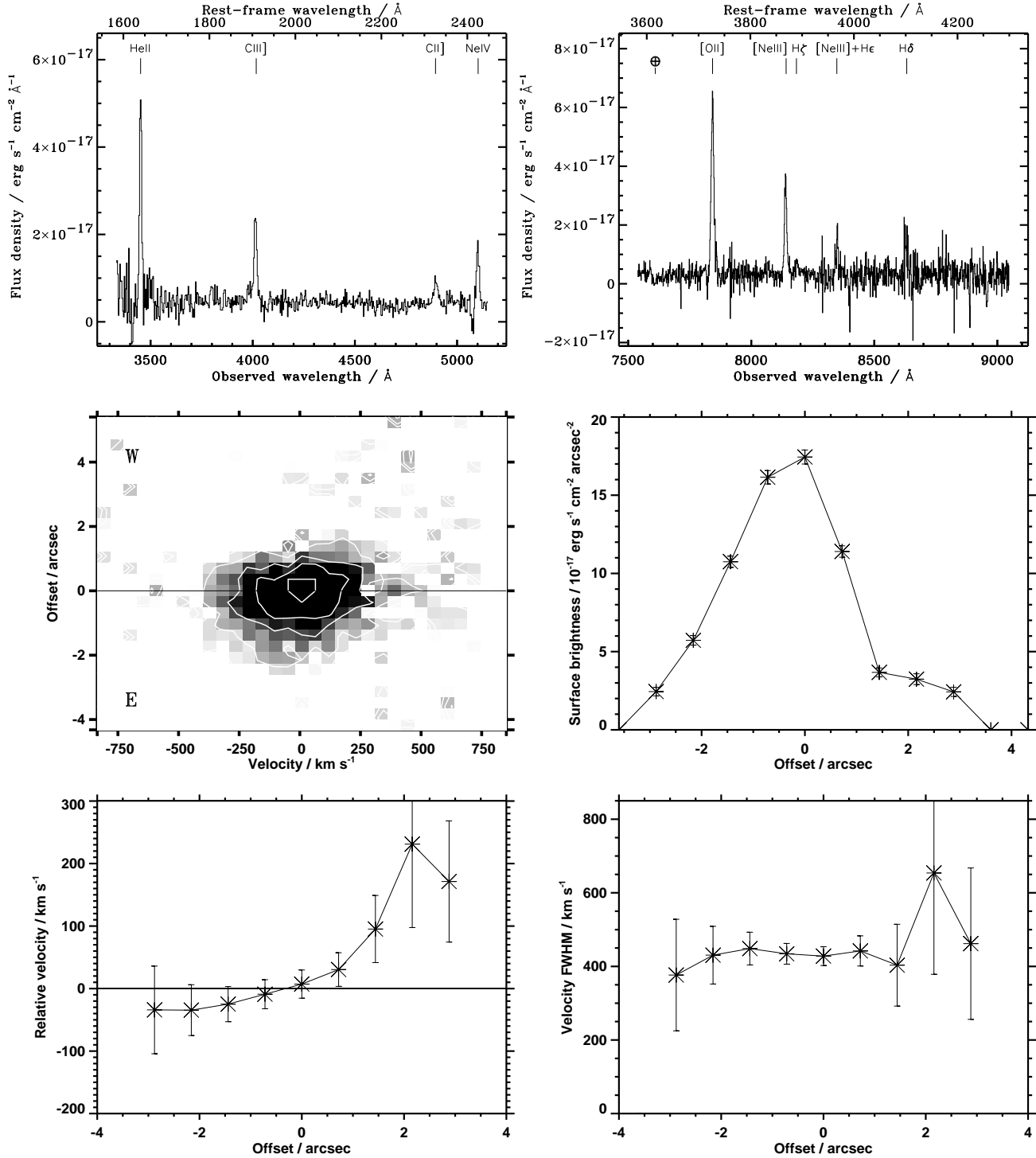


Figure 6. The spectroscopic data for 3C252. Details as in Figure 2.

sorption feature is readily apparent in the red-arm spectrum (Figure 5b).

3C252 shows line emission extended over only a few arcseconds, with a smooth velocity profile again representing simple rotation or infall/outflow (Figure 6). The galaxy has the lowest velocity FWHM of any source in the sample, although still with a velocity dispersion significantly greater than the mean relative velocities. The integrated [OII] 3727

flux is amongst the lowest in the sample, but many of the other emission lines are strong by comparison.

3C265 is an extreme radio galaxy in both its continuum and emission line properties. More than a magnitude brighter at optical wavelengths than other radio galaxies at the same redshift, its continuum emission is composed of a large number of components extending over 80 kpc (10 arcsec) with a remarkably blue colour (Figure 7a); its [OII] 3727

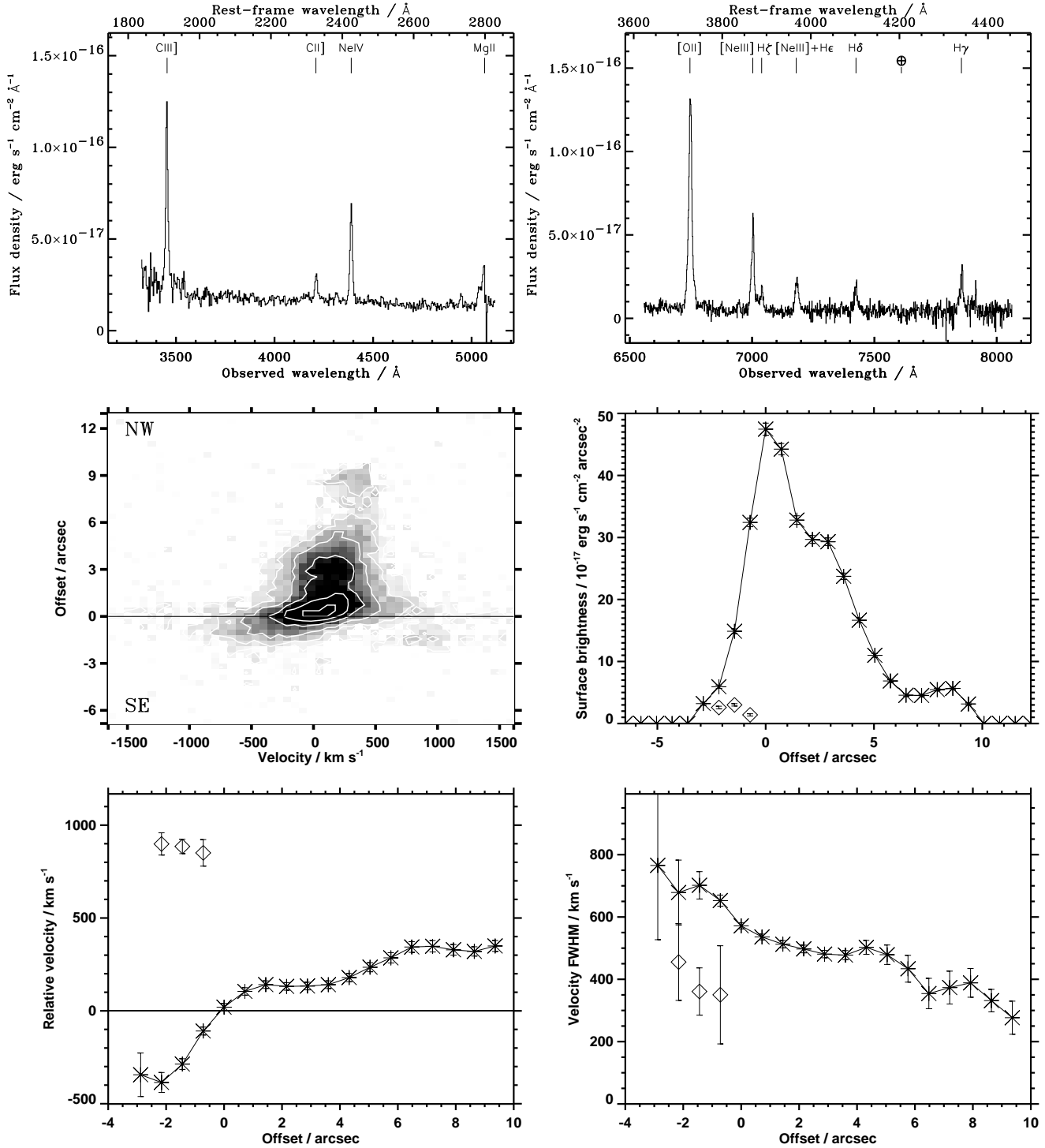


Figure 7. The spectroscopic data for 3C265. Details as in Figure 2.

emission shows a similar, or even greater, extent (Figure 7; see also Tadhunter 1991; Rigler et al. 1992; McCarthy et al. 1995, 1996; Dey & Spinrad 1996). From the galaxy centre the emission extends a considerable distance to the north-west with a fairly flat velocity profile and decreasing velocity width. The ‘blob’ of line emission offset 9 arcsec to the north-west of the galaxy centre is associated with a continuum emission region (e.g. see Best et al. 1997). The prop-

erties of the [OII] 3727 emission line are also observed with lower signal-to-noise in weaker emission lines.

Tadhunter (1991) reported the presence of high velocity gas components to the south-east of the nucleus, with velocities of +750 and +1550 km s<sup>-1</sup> with respect to the velocity at the continuum centroid, although these were not obvious in the data of Dey & Spinrad (1996) nor of McCarthy et al. (1996). The current data confirm the pres-

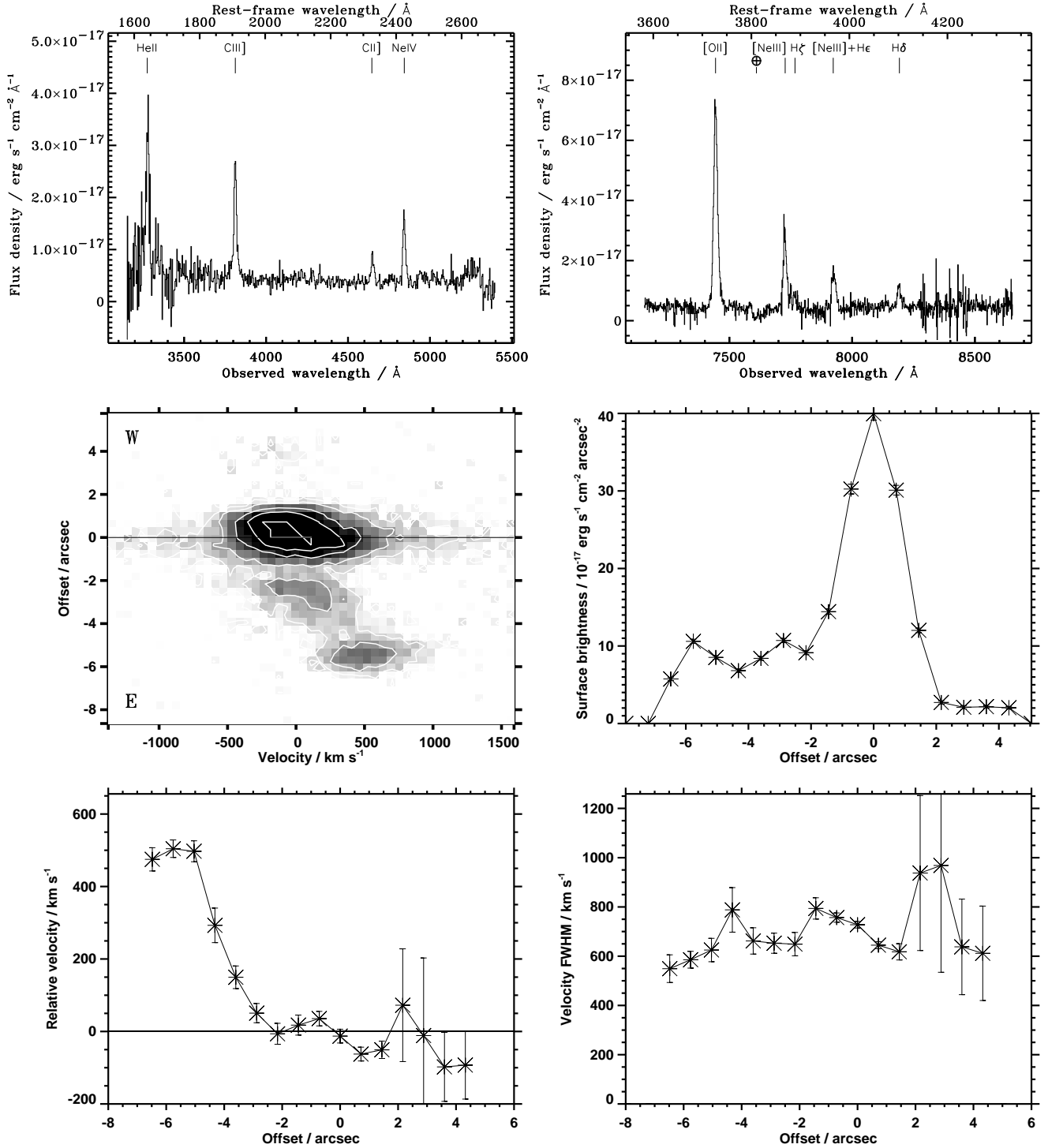


Figure 8. The spectroscopic data for 3C280. Details as in Figure 2.

ence of the  $+750 \text{ km s}^{-1}$  component, the slightly higher velocity measured here being due to a small offset between the continuum centroid position determined here and that of Tadhunter. This component is also detected clearly in the [NeIII] 3869 line. The  $+1550 \text{ km s}^{-1}$  component is, however, not detected; this may be due to the difference in slit position angle of the two observations ( $136^\circ$  versus  $145^\circ$ ) and/or the use of a narrower slit in the current observations. The

origin of the high velocity component is almost certainly related to the radio source activity (Tadhunter 1991).

3C280 has a complex emission line structure extending over 11 arcsec (90 kpc; Figure 8). The emission shows a strong central peak together with a large extension to the east where it forms a loop around the eastern radio lobe (Rigler et al. 1992; McCarthy et al. 1995). This loop of emission is redshifted with respect to the velocity at the

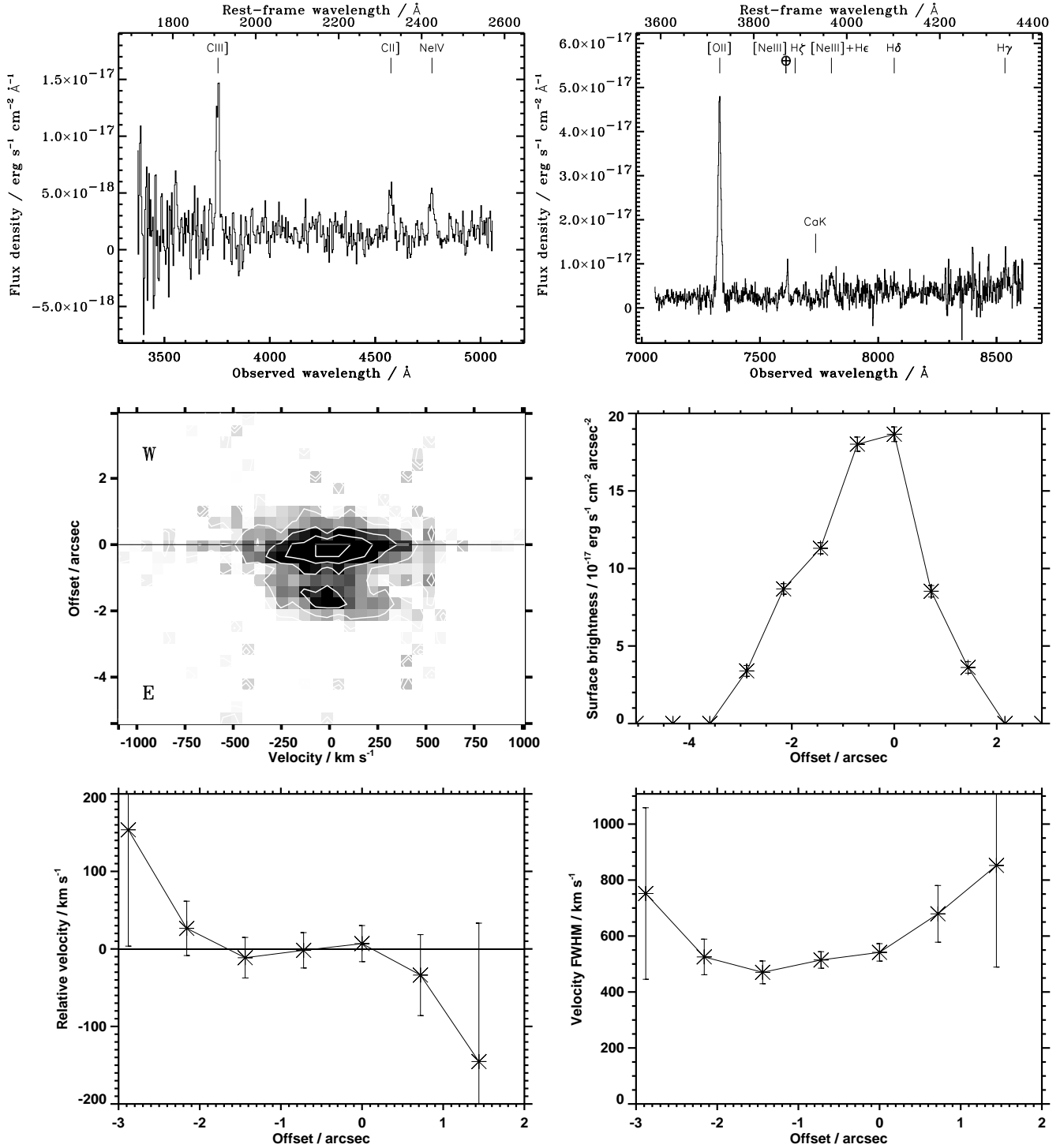


Figure 9. The spectroscopic data for **3C289**. Details as in Figure 2.

continuum centroid by about  $500 \text{ km s}^{-1}$ . The FWHM of the [OII] 3727 emission is moderately high and almost constant throughout the entire extent of the emission.

**3C289** shows a central peak of line emission, with a secondary emission region a couple of arcseconds to the south-east (Figure 9; see also Rigler et al. 1992), corresponding to a faint emission region on the HST image of Best et al. (1997). Both the integrated [OII] 3727 emission line intensity

and the FWHM of the emission line are relatively low for the sample. The velocity profile could represent rotation or infall/outflow of material. A weak CaK 3933Å absorption line may be present in the red-arm spectrum.

**3C324** has previously been described as showing a velocity shear of  $700 \text{ km s}^{-1}$  along the radio axis (Spinrad & Djorgovski 1984; McCarthy et al. 1996), but the higher spectral and spatial resolution data presented in Figure 10

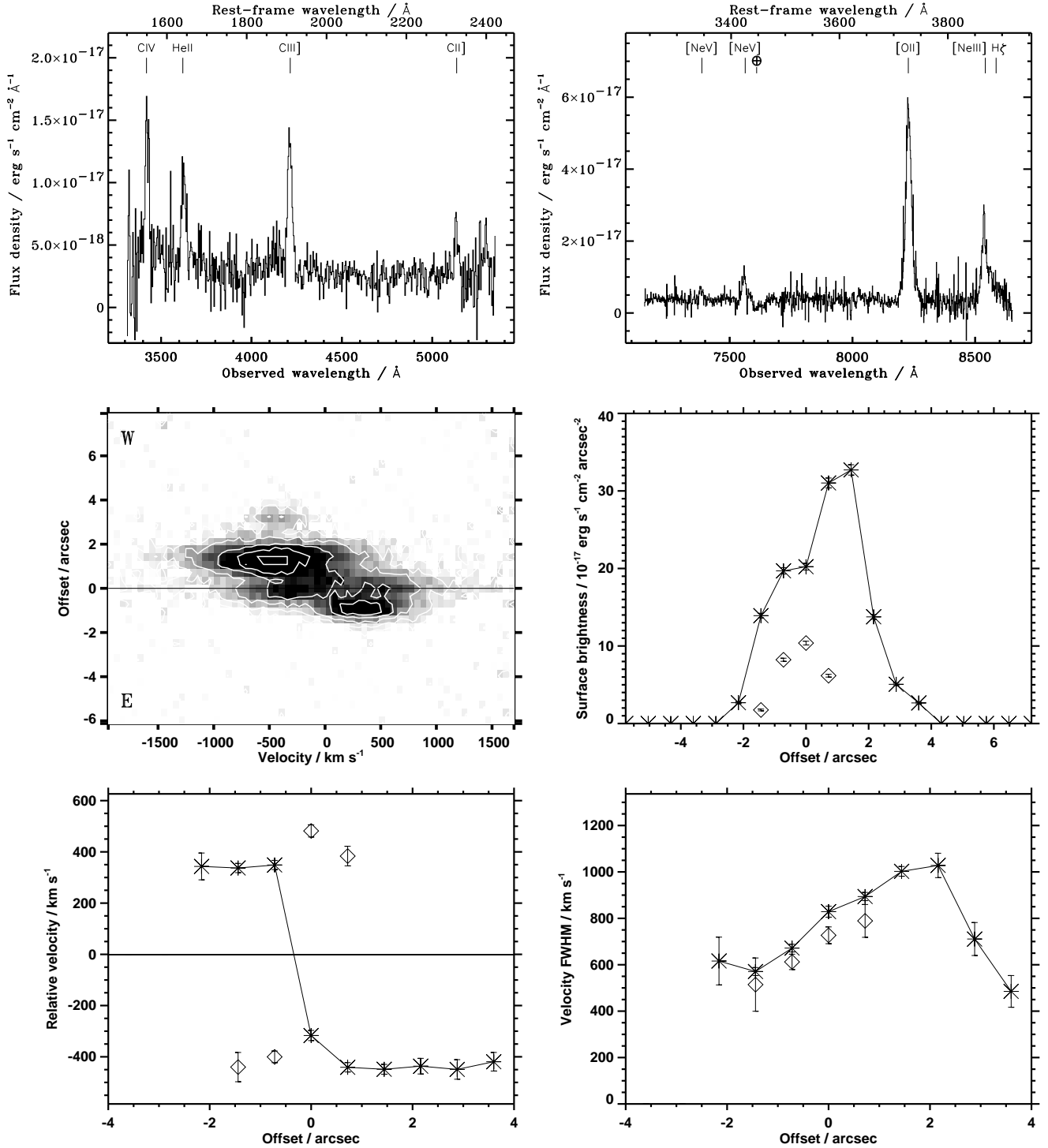


Figure 10. The spectroscopic data for 3C324. Details as in Figure 2.

clearly indicate that that is not the case. The emission line gas is composed of two distinct components, with velocities separated by  $\sim 800 \text{ km s}^{-1}$ . At the position corresponding to the continuum centroid, the two velocity components overlap; the adoption of the mean of these two as the true redshift of the system is necessarily uncertain, and the possibility that the true centre of 3C324 lies coincident with either of the components determined here to be at  $+400$

and  $-400 \text{ km s}^{-1}$  cannot be excluded. The western emission line component is slightly more luminous and has the higher FWHM, reaching over  $1000 \text{ km s}^{-1}$ ; note that the dissociation of the central emission into two separate components means that a FWHM as high as  $1500 \text{ km s}^{-1}$ , determined by McCarthy et al. (1996) for the blended pair, is not measured here. It is unclear whether these two emission line regions represent different physical systems, perhaps undergoing a

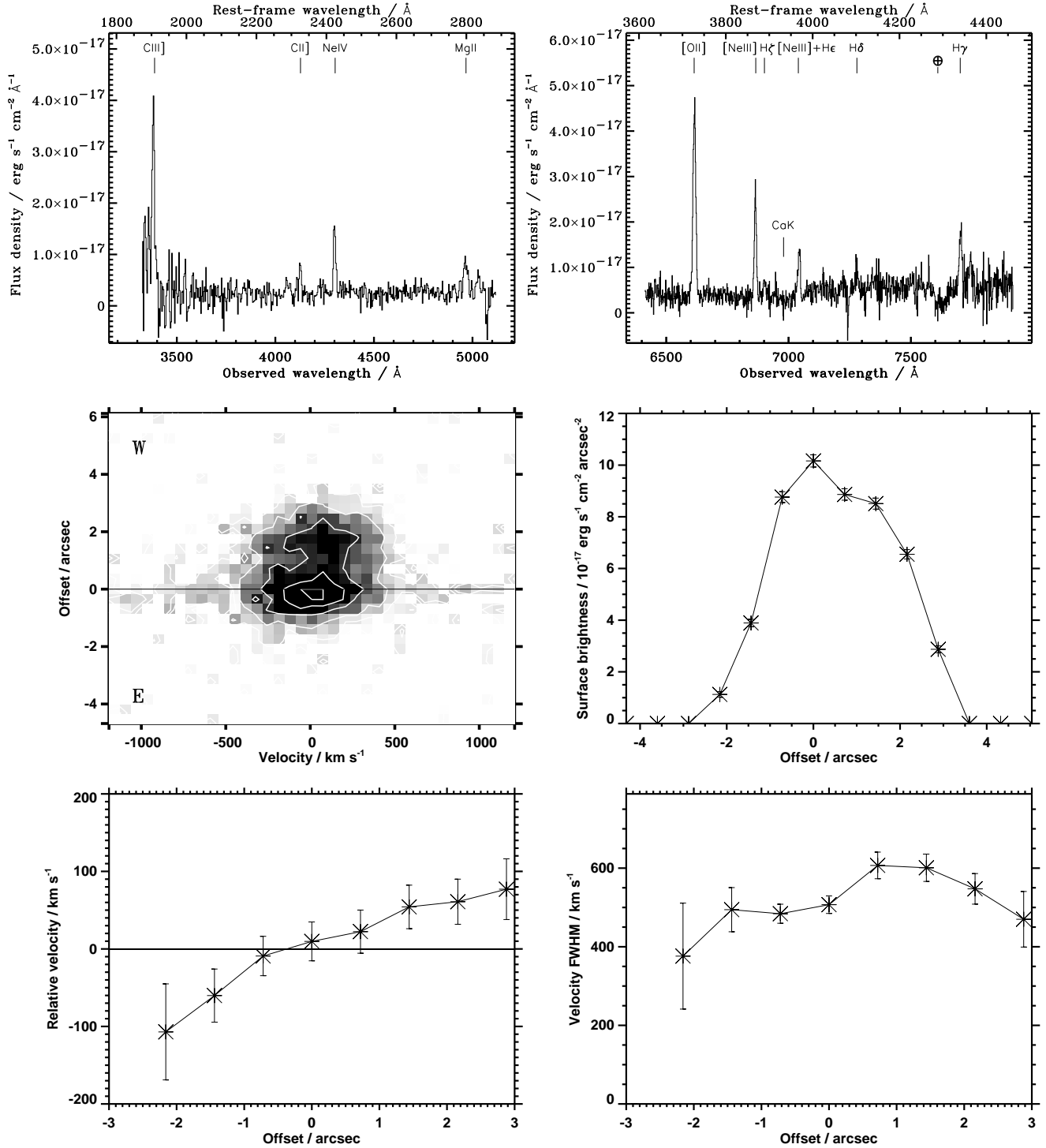


Figure 11. The spectroscopic data for 3C340. Details as in Figure 2.

merger, or whether radial acceleration by radio jet shocks is responsible for the bimodality of the emission line velocities.

This two component structure of the emission line properties of 3C324 reflects the structure of its optical–UV continuum emission (Longair et al. 1995; Dickinson et al. 1996). The HST images show bright emission regions to the east and west, but a central minimum corresponding to the radio core position and interpreted as extinction by a central dust

lane. Narrow-band images of the [OII] 3727 emission line also show an elongated clumpy morphology (Hammer & Le Fèvre 1990; Rigler et al. 1992). Cimatti et al. (1996) showed that the polarisation properties of the emission to the east and the west of the nucleus also differ strongly.

3C340 is another radio galaxy whose emission line structure is smooth and well-ordered (Figure 11). The relative velocity plot is consistent with simple rotation or infall



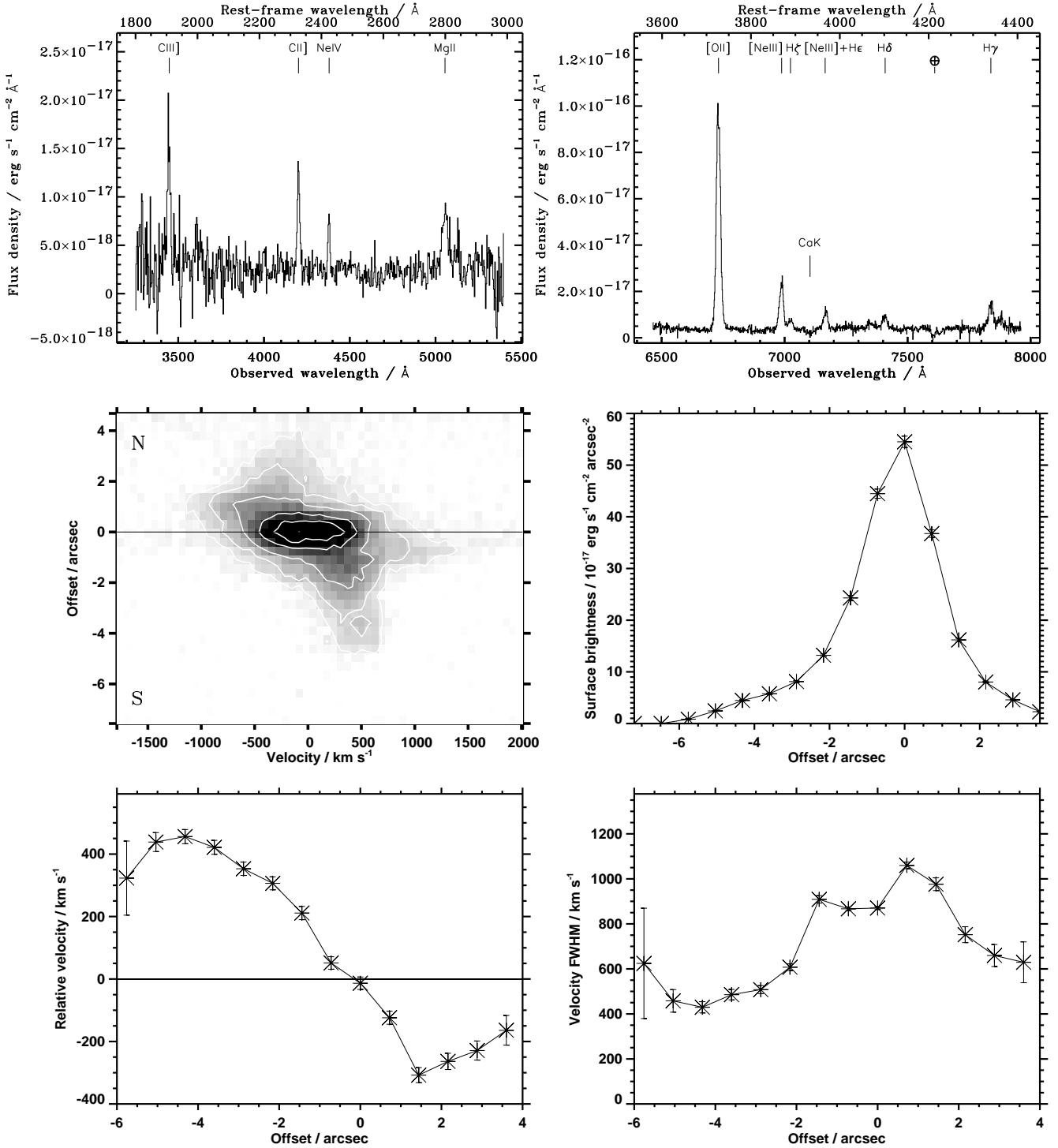
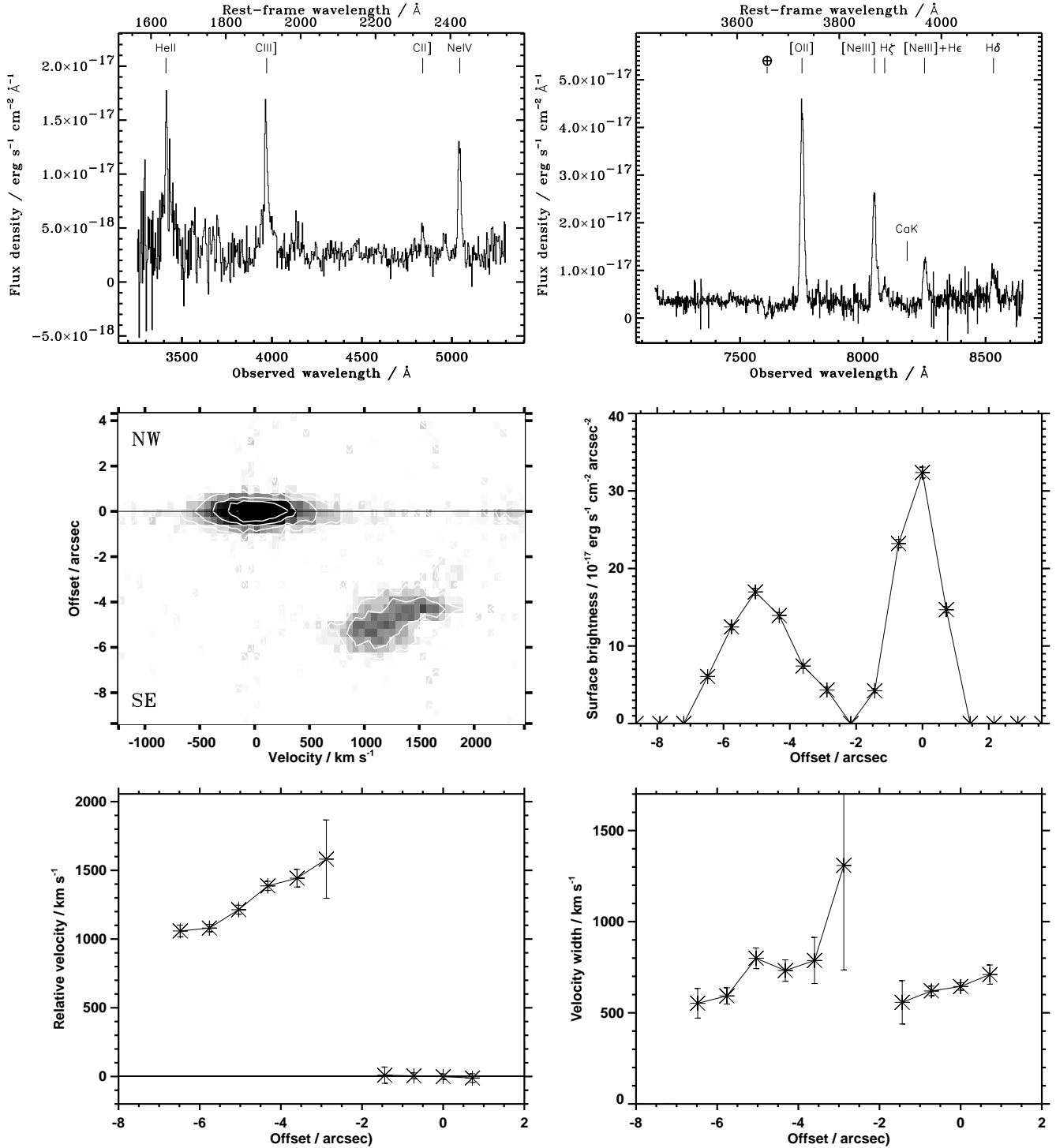


Figure 12. The spectroscopic data for 3C352. Details as in Figure 2.

or outflow of material, and the line widths are the second lowest in the sample. The emission is centrally concentrated, with a small (2 to 3 arcsec) extension along the radio axis to the west (see also the narrow-band image of McCarthy et al. 1995). The integrated [OII] 3727 intensity is relatively low, with the emission line ratios in the spectrum indicating a very high ionisation state. The galaxy shows a significant 4000Å break ( $1.52 \pm 0.07$ ), a broad CaK 3933Å absorption

feature, and a red colour for its short wavelength continuum emission.

3C352 shows an elongated [OII] 3727 emission region extending for 10 arcseconds, and possibly further since the presence of a bright star to the north prohibits the detection of any further line emission in that direction. The velocity profile is smooth throughout the central regions of the source with a velocity shear exceeding  $700 \text{ km s}^{-1}$ , but dis-



**Figure 13.** The spectroscopic data for **3C356**. Details as in Figure 2. The plotted one-dimensional spectra are for the northern galaxy.

torts somewhat at larger distances (Figure 12). The FWHM is large, reaching over  $1000 \text{ km s}^{-1}$ . These results are consistent with those of Hippelein and Meisenheimer (1992) from Fabry–Perot imaging. Relative to the rest of the sample, the lower ionisation lines are strong in the spectrum. A broad CaK absorption feature can be seen at  $3933 \text{ \AA}$ .

**3C356** has long been a puzzle, with two equally bright infrared galaxies separated by about 5 arcsec corresponding

to the location to two radio core-like features. The identification of the true nucleus has been a matter of some debate, with different authors favouring the northern or the southern galaxy for different reasons (see Best et al 1997 for a more complete discussion). For the current data, the slit was placed to include both components, with zero offset corresponding to the location of the northern galaxy (see Figure 13). As is observed for the continuum emission (e.g.

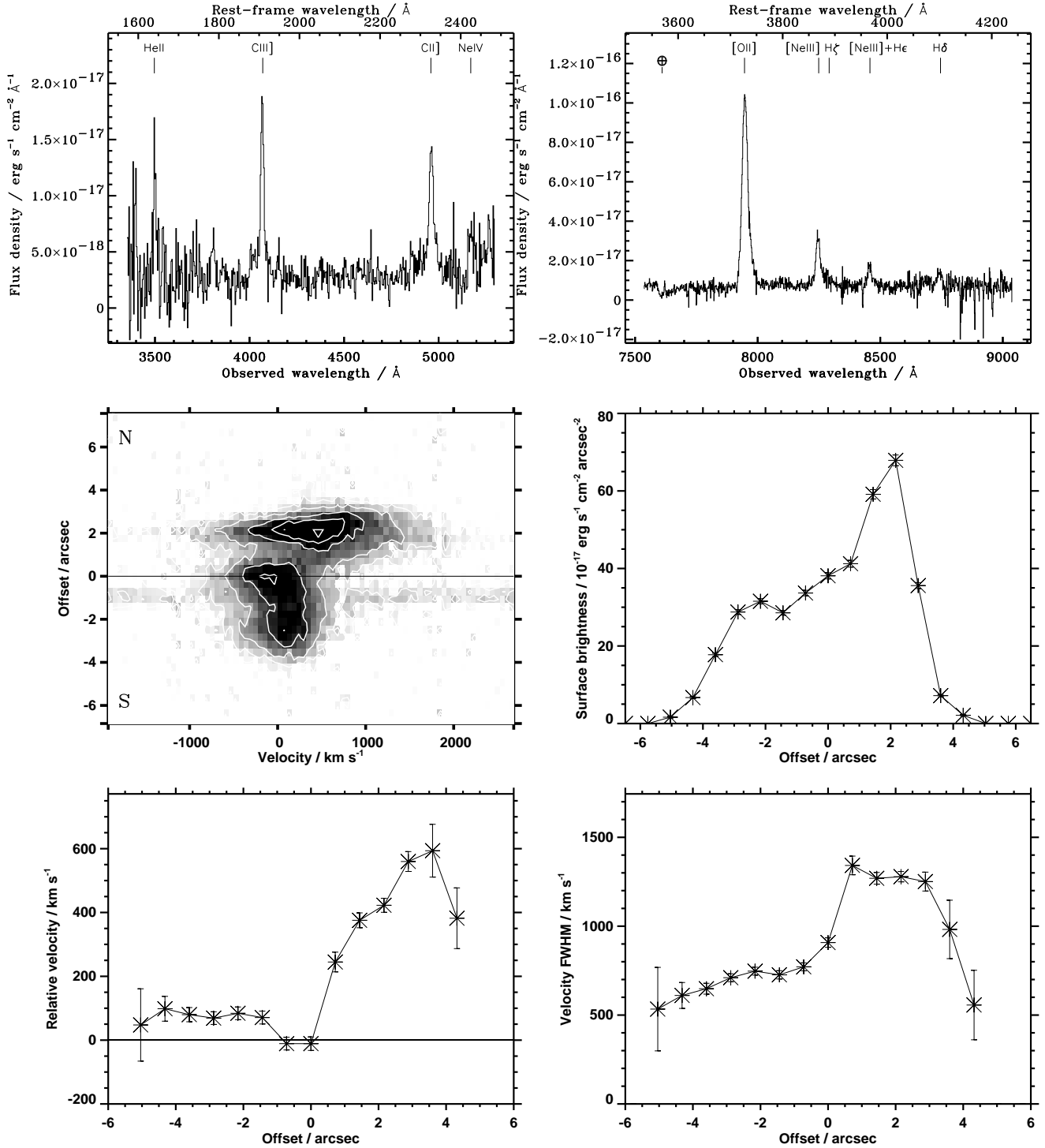


Figure 14. The spectroscopic data for 3C368. Details as in Figure 2.

Rigler et al. 1992, Best et al. 1997), the line emission from the northern region is compact whilst that from the southern region is more extended but gives a comparable integrated intensity (see also Lacy & Rawlings 1994, McCarthy et al. 1996). The northern region shows virtually no variation in its velocity with position, and a low velocity width; the southern region, redshifted by about  $1200 \text{ km s}^{-1}$ , shows

a steep velocity shear of  $500 \text{ km s}^{-1}$  in 3 arcsec and a slightly broader FWHM.

3C368 is easily the best-studied galaxy in this sample (e.g. Hammer et al. 1991, Meisenheimer & Hippelein 1992, Rigler et al. 1992, Dickson et al. 1995, Longair et al. 1995, McCarthy et al. 1995, 1996, Stockton et al. 1996, Best et al. 1997, 1998a to name only the most recent), showing a highly elongated morphology in both its continuum and line

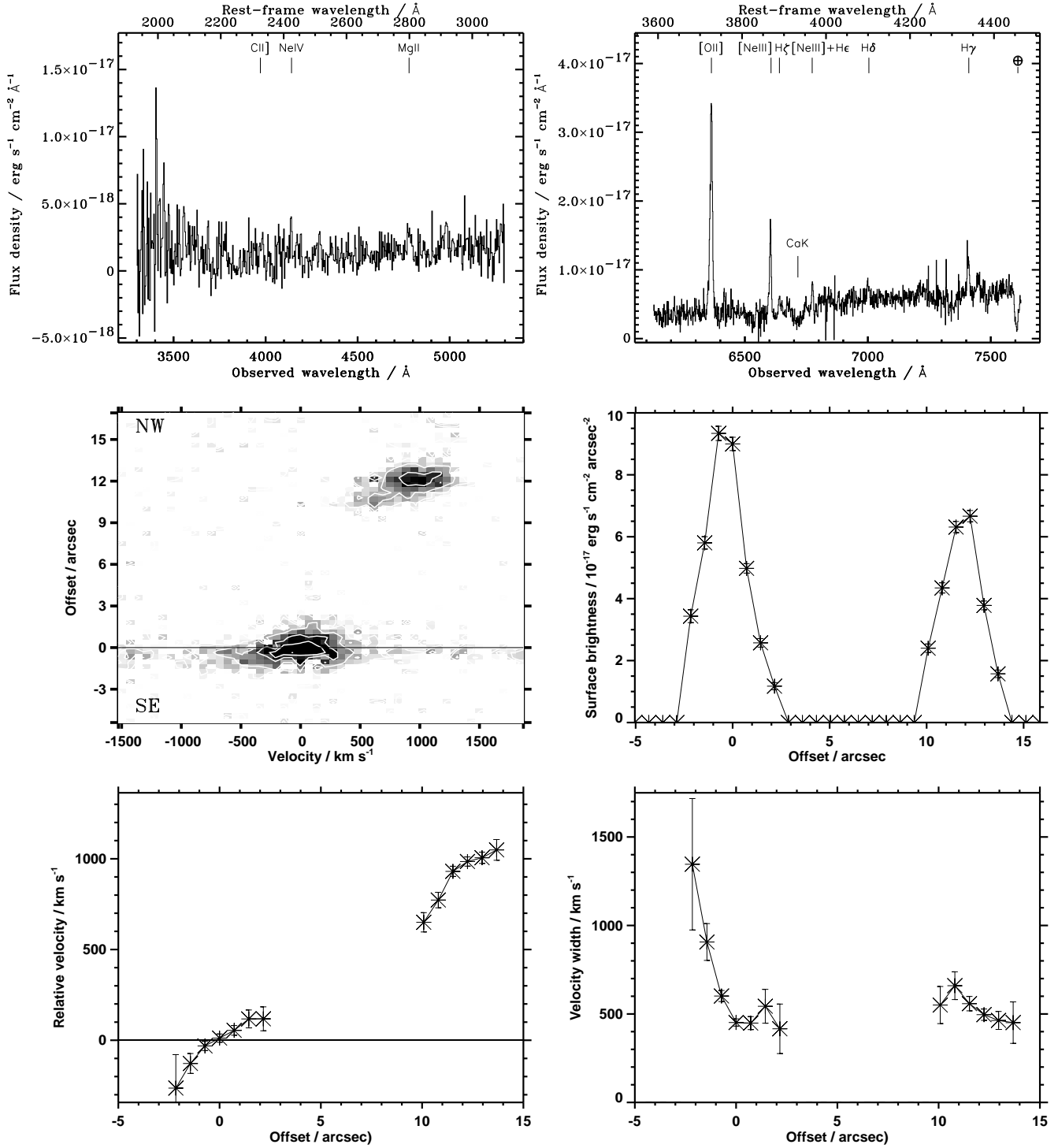


Figure 15. The spectroscopic data for 3C441. Details as in Figure 2.

emission extending about 10 arcsec (Figure 14), comparable to the extent of the radio source. The velocity structure of the line emission determined here is in full agreement with the previous lower spectral resolution measurements and the Fabry–Perot imaging of Meisenheimer & Hippelein (1992), the northern knots showing a velocity offset of order  $600 \text{ km s}^{-1}$  and an extreme FWHM (up to  $1350 \text{ km s}^{-1}$ ). Many of the lower ionisation lines in the spectrum appear

strong relative to the other galaxies in the sample. Study of the continuum emission is hampered by the presence of a galactic M–dwarf star lying within a couple of arcseconds of the centre of 3C368. (Hammer et al. 1991).

3C441 shows, in addition to the [OII] 3727 emission from the central galaxy, a secondary region of emission offset 12 arcseconds to the north–west and about  $800 \text{ km s}^{-1}$  redwards in velocity (Figure 15; cf. McCarthy et al. 1996,

Lacy et al. 1998). This emission region lies close to the radio hotspot (McCarthy et al. 1995) and has been associated with an interaction between the radio jet and a companion galaxy to 3C441 (Lacy et al. 1998). The [OII] 3727 emission associated with the host galaxy itself has a low integrated intensity and a smooth velocity gradient of nearly  $400 \text{ km s}^{-1}$  in 5 arcsec, consistent with rotation or with infalling / outflowing gas. A relatively large  $4000\text{\AA}$  break is observed in the spectrum ( $1.64 \pm 0.04$ ), together with strong CaK  $3933\text{\AA}$  absorption, consistent with the fact that this galaxy also shows only a very weak alignment effect at optical–UV wavelenths (Best et al. 1997).

Composite spectra have been produced for each of the red and blue arms of the spectrograph, by combining all of the presented spectra at the same rest–frame wavelengths, giving each individual spectrum an equal weighting. 3C368 was excluded from this combined spectrum due to the contribution of the foreground M–star to its emission. The resulting total spectra, shown in Figure 16, are equivalent to single spectra of over 20 hours in duration. In Table 3 are tabulated the relative strengths of the emission lines in this composite spectrum. These are quoted relative to the commonly adopted scale of  $H\beta = 100$  by assuming  $H\gamma/H\beta \approx 0.47$ , appropriate for Case B recombination at  $T=10000 \text{ K}$  (Osterbrock 1989); this value is also consistent with that obtained from the  $H\delta$  line assuming  $H\delta/H\beta \approx 0.26$ .

One feature is immediately apparent when comparing these relative line fluxes with those from the composite spectrum of radio galaxies with redshifts  $0.1 < z < 3$  constructed by McCarthy (1993): the emission lines at short wavelengths are less luminous by factors of 2 to 4, relative to  $H\beta$ , than those of McCarthy’s spectrum. This may be due to the wide range of redshifts of the radio galaxies making up McCarthy’s composite and the strong correlation between emission line flux and redshift (Rawlings & Saunders 1991); the shortest wavelength lines in his composite spectrum are only observed in the highest redshift sources (with powerful line emission) whilst the  $H\beta$  line is seen in the lower redshift sources, introducing a bias towards lines at shorter rest–frame wavelengths appearing more luminous. The composite spectra presented in Figure 16 and Table 3 are much less prone to this bias, and so provide a fairly accurate measure of relative line fluxes at redshift  $z \sim 1$ .

Besides the emission lines, other features visible in the spectra include the broad CaK absorption feature at  $3933\text{\AA}$ , with an equivalent width of  $10 \pm 2\text{\AA}$ , and a weaker G–band absorption at  $4300\text{\AA}$  with an equivalent width of  $7 \pm 3\text{\AA}$ . A  $4000\text{\AA}$  break is marginally visible, but there is little evidence for the spectral breaks at  $2640$  and  $2900\text{\AA}$  (cf. Spinrad et al. 1997) expected from an old stellar population. This is not too surprising since the contribution from the old stars to the total flux density at these wavelengths, and indeed throughout all of the combined blue arm spectrum, is small compared to that of the aligned emission.

## 4 CONCLUSIONS

Extremely deep spectroscopic observations have been presented of an unbiased sample of the most powerful radio galaxies with redshifts  $z \sim 1$ . A broad range of emission

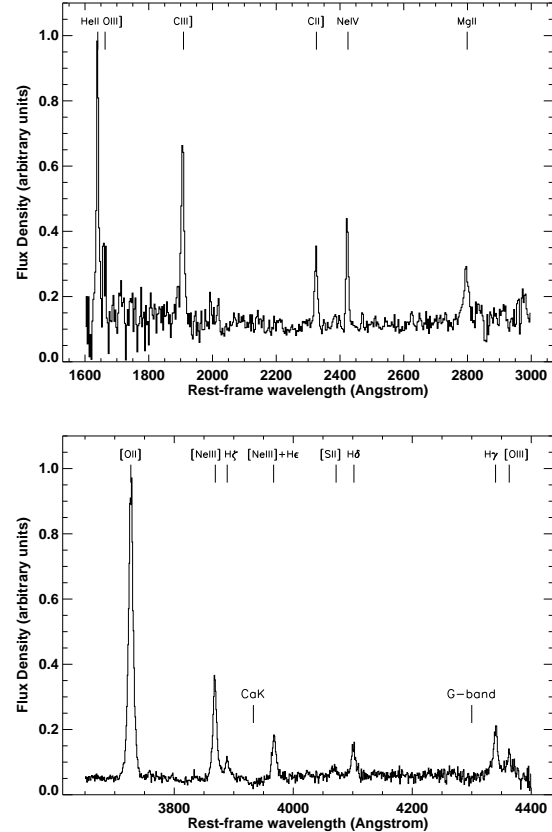


**Figure 16.** A summation of the spectra for all of the radio galaxies.

**Table 3.** Emission line fluxes of the ‘average’ spectrum of the 3CR radio galaxies, relative to  $H\beta = 100$ .

Line	Flux	Line	Flux
HeII 1640	95	[NeIII] 3869	65
OIII] 1663	19	Hζ 3889	12
CIII] 1909	83	Hε + [NeIII] 3967	26
CII] 2326	27	[SII] 4072	9
[NeIV] 2425	33	Hδ 4102	24
MgII 2798	38	Hγ 4340	47
[OII] 3727	256	[OIII] 4363	21

lines is seen and a study at intermediate spectral resolution of the two–dimensional velocity structures of the emission line gas are presented. The enhanced sensitivity of new CCDs at short wavelengths has enabled the measurement of emission line ratios and continuum flux densities at unprecedentedly short wavelengths,  $\lambda \lesssim 3500\text{\AA}$ , corresponding to the near–UV in the rest–frame of the sources where any continuum contribution from an evolved stellar population will be negligible.

The main results can be summarised as follows:

- Analysis of the velocity structures of these galaxies shows them to exhibit a wide range of kinematics. Some sources have highly distorted velocity profiles and velocity FWHM exceeding  $1000 \text{ km s}^{-1}$ . Other sources have lower velocity dispersions and more ordered emission line profiles, with the variation of mean velocity along the slit be-

ing consistent with simple rotation. Even in these latter sources, however, the velocity FWHM are still a few hundred  $\text{km s}^{-1}$ , significantly larger than the variations in mean velocities, indicating that there is considerable scatter in the emission line cloud velocities relative to any mean rotational motion.

- A high velocity ( $\sim 750 \text{ km s}^{-1}$ ) gas component is confirmed close to the nucleus of 3C265. This is unique amongst the sample, but other galaxies display gas with velocities  $\gtrsim 400 \text{ km s}^{-1}$  offset a few arcseconds from the centre, either connected to the central emission line region (3C280, 3C352, 3C368) or as a discrete region (3C356, 3C441).

- 3C324 is shown to consist of two kinematically distinct components separated in velocity by  $800 \text{ km s}^{-1}$ .

- For those galaxies in which the alignment effect is seen to be relatively weak in the HST images, and hence the spectra are not dominated by emission from these alignment processes,  $4000\text{\AA}$  breaks from evolved stellar populations are clearly visible. CaK absorption features are also readily apparent in a number of the spectra.

- At rest-frame wavelengths shortward of  $\sim 2500\text{\AA}$  the continuum emission of the galaxies is, on average, relatively flat in  $f_\lambda$ , although considerable source to source variations are seen both in these continuum colours and in the emission line ratios.

- A composite spectrum gives the relative strengths of the emission lines at rest-frame wavelengths between HeII 1640 and [OIII] 4363. Emission lines at short rest-frame wavelengths are systematically weaker (relative to  $H\beta$ ) than those in the composite spectrum of McCarthy (1993). It is suspected that this is due to a bias introduced in McCarthy's spectrum by the emission line strength versus redshift correlation, and the large redshift coverage of the radio galaxies which comprise his sample.

The broad variation in kinematical and ionisation properties within the sample as a whole are investigated and compared against other radio source properties in the accompanying Paper 2, and conclusions are drawn there concerning the origin of the ionisation and kinematics of the emission line gas.

## ACKNOWLEDGEMENTS

This work was supported in part by the Formation and Evolution of Galaxies network set up by the European Commission under contract ERB FMRX-CT96-086 of its TMR programme. The William Herschel Telescope is operated on the island of La Palma by the Isaac Newton Group in the Spanish Observatorio del Roches de los Muchachos of the Instituto de Astrofísica de Canarias. We thank the referee, Mike Dopita, for his careful consideration of the original manuscript and a number of useful suggestions.

## REFERENCES

Barthel P. D., 1989, *ApJ*, 336, 606  
 Baum S. A., Heckman T. M., 1989, *ApJ*, 336, 681  
 Baum S. A., Heckman T. M., van Breugel W. J. M., 1992, *ApJ*, 389, 208

Baum S. A., McCarthy P. J., O'Dea C. P., 1998, in Röttgering H. J. A., Best P. N., Lehnert M. D., eds, *The most distant radio galaxies*. Royal Netherlands Acad. Arts & Sci., Amsterdam, p. 97  
 Best P. N., Carilli C. L., Garrington S. T., Longair M. S., Röttgering H. J. A., 1998a, *MNRAS*, 299, 357  
 Best P. N., Longair M. S., Röttgering H. J. A., 1996, *MNRAS*, 280, L9  
 Best P. N., Longair M. S., Röttgering H. J. A., 1997, *MNRAS*, 292, 758  
 Best P. N., Longair M. S., Röttgering H. J. A., 1998b, *MNRAS*, 295, 549  
 Best P. N., Röttgering H. J. A., Longair M. S., 1999, *MNRAS*: submitted.  
 Bicknell G. V., Dopita M. A., O'Dea C. P., 1997, *ApJ*, 485, 112  
 Bruzual G., 1983, *ApJ*, 273, 105  
 Burstein D., Heiles C., 1982, *AJ*, 87, 1165  
 Chambers K. C., Miley G. K., van Breugel W. J. M., 1987, *Nat*, 329, 604  
 Cimatti A., Dey A., van Breugel W., Antonucci R., Spinrad H., 1996, *ApJ*, 465, 145  
 Clark N. E., Axon D. J., Tadhunter C. N., Robinson A., O'Brien P., 1998, *ApJ*, 494, 546  
 Crawford C. S., Fabian A. C., 1996, *MNRAS*, 282, 1483  
 Dey A., Spinrad H., 1996, *ApJ*, 459, 133  
 Dickinson M., Dey A., Spinrad H., 1996, in Hippelein H., Meisenheimer K., Röser H.-J., eds, *Galaxies in the Young Universe*. Springer Verlag, p. 164  
 Dickson R., Tadhunter C., Shaw M., Clark N., Morganti R., 1995, *MNRAS*, 273, L29  
 Dunlop J. S., Peacock J., 1993, *MNRAS*, 263, 936  
 Economou F., Lawrence A., Ward M. J., Blanco P. R., 1995, *MNRAS*, 272, L5  
 Hammer F., Le Fèvre O., 1990, *ApJ*, 357, 38  
 Hammer F., Le Fèvre O., Proust D., 1991, *ApJ*, 374, 91  
 Heckman T. M., Smith E. P., Baum S. A., van Breugel W. J. M., Miley G. K., Illingworth G. D., Bothun G. D., Balick B., 1986, *ApJ*, 311, 526  
 Hippelein H., Meisenheimer K., 1992, *A&A*, 264, 472  
 Howarth I. D., 1983, *MNRAS*, 203, 301  
 Lacy M., Rawlings S., 1994, *MNRAS*, 270, 431  
 Lacy M., Rawlings S., Blundell K. M., Ridgway S. E., 1998, *MNRAS*, 298, 966  
 Laing R. A., Riley J. M., Longair M. S., 1983, *MNRAS*, 204, 151  
 Lilly S. J., Longair M. S., 1984, *MNRAS*, 211, 833  
 Longair M. S., Best P. N., Röttgering H. J. A., 1995, *MNRAS*, 275, L47  
 McCarthy P. J., 1988, Ph.D. thesis, University of California, Berkeley  
 McCarthy P. J., 1993, *ARA&A*, 31, 639  
 McCarthy P. J., Baum S. A., Spinrad H., 1996, *ApJ Supp.*, 106, 281  
 McCarthy P. J., Spinrad H., van Breugel W. J. M., 1995, *ApJ Supp.*, 99, 27  
 McCarthy P. J., van Breugel W. J. M., Spinrad H., Djorgovski S., 1987, *ApJ*, 321, L29  
 Meisenheimer K., Hippelein H., 1992, *A&A*, 264, 455  
 Neeser M. J., Hippelein H., Meisenheimer K., 1997, *ApJ*, 491, 522  
 Osterbrock D. E., 1989, *Astrophysics of Gaseous Nebulae and Active Galactic Nuclei*. Mill Valley CA: University Science Books  
 Rawlings S., Lacy M., Sivia D. S., Eales S. A., 1995, *MNRAS*, 274, 428  
 Rawlings S., Saunders R., 1991, *Nat*, 349, 138  
 Rigler M. A., Lilly S. J., Stockton A., Hammer F., Le Fèvre O., 1992, *ApJ*, 385, 61  
 Robinson A., Binette L., Fosbury R. A. E., Tadhunter C. N., 1987, *MNRAS*, 227, 97

- Röttgering H. J. A., Miley G. K., 1996, in Bergeron J., ed., The Early Universe with the VLT. Springer Verlag, p. 285
- Spinrad H., 1982, PASP, 94, 397
- Spinrad H., Dey A., Stern D., Dunlop J., Peacock J., Jimenez R., Windhorst R., 1997, ApJ, 484, 581
- Spinrad H., Djorgovski S., 1984, ApJ, 280, L9
- Stockton A., Ridgway S. E., Kellogg M., 1996, AJ, 112, 902
- Tadhunter C. N., 1991, MNRAS, 251, 46P
- van Breugel W. J. M., Miley G. K., Heckman T. M., Butcher H., Bridle A., 1985, ApJ, 290, 496
- Villar-Martín M., Tadhunter C., Morganti R., Axon D., Koeke-moer A., 1999, MNRAS, 307, 24